The Application of Computational Fluid Dynamics in an Andersen Cascade Impactor for Pharmaceutical Aerosols

Janwit Dechraksa

A Thesis Submitted in Partial Fulfillment of the Requirements for the Degree of Doctor of Philosophy in Pharmaceutical Sciences

Prince of Songkla University

2016

The Application of Computational Fluid Dynamics in an Andersen Cascade Impactor for Pharmaceutical Aerosols

Janwit Dechraksa

A Thesis Submitted in Partial Fulfillment of the Requirements for the Degree of Doctor of Philosophy in Pharmaceutical Sciences

Prince of Songkla University

2016

Thesis Title The application of computational fluid dynamics in an Andersen cascade impactor for pharmaceutical aerosols

Author Mr. Janwit Dechraksa

Major Program Pharmaceutical Sciences

Major Advisor

.....
(Assoc. Prof. Dr. Teerapol Srichana)

Examining Committee:

.....Chairperson
(Assoc. Prof. Dr. Damrongsak Faroongsarng)

.....Committee
(Assoc. Prof. Dr. Teerapol Srichana)

.....Committee
(Assoc. Prof. Wibul Wongpoowarak)

.....Committee
(Dr. Chonladda Pitchayajittipong)

The Graduate School, Prince of Songkla University, has approved this thesis as partial fulfillment of the requirements for the Doctor of Philosophy Degree in Pharmaceutical Sciences

.....
(Assoc. Prof. Dr. Teerapol Srichana)
Dean of Graduate School

This is to certify that the work here submitted is the result of the candidate's own investigations. Due acknowledgement has been made of any assistance received.

.....Signature

(Assoc. Prof. Dr. Teerapol Srichana)

Major Advisor

.....Signature

(Mr. Janwit Dechraksa)

Candidate

I hereby certify that this work has not been accepted in substance for any degree, and is not being currently submitted in candidature for any degree.

.....Signature

(Mr. Janwit Dechraksa)

Candidate

ชื่อเรื่องวิทยานิพนธ์ การประยุกต์ใช้แบบจำลองพลศาสตร์การไหลด้วยคอมพิวเตอร์ในเครื่องแอนเดอร์เซน คาสเคด อิมแพคเตอร์ สำหรับเภสัชภัณฑ์แอโรโซล

ผู้เขียน เจนวิทย์ เดชรักษา

สาขาวิชา เภสัชศาสตร์

ปีการศึกษา 2558

บทคัดย่อ

การกระจายขนาดอนุภาคเป็นตัวแปรสำคัญในการพัฒนาตำรับเภสัชภัณฑ์แอโรโซล โดยปัจจุบันมีเครื่องมือหลายชนิดที่สามารถใช้ในการประเมินขนาดอนุภาค แอนเดอร์เซน คาสเคด อิมแพคเตอร์ (เอซีไอ) เป็นเครื่องมือมาตรฐานที่ใช้ในการประเมินการกระจายขนาดอนุภาคขณะลอยตัวอยู่ในอากาศ โดยมีค่าขนาดเส้นผ่านศูนย์กลางเฉลี่ยเป็นตัวแทนการกระจายขนาดอนุภาคของเภสัชตำรับนั้น ซึ่งเอซีไอถูกออกแบบมาเพื่อการศึกษาด้านมลภาวะทางอากาศ แต่มีการนำมาประยุกต์ใช้ในงานเภสัชศาสตร์อย่างแพร่หลาย เพื่อควบคุมคุณภาพเภสัชภัณฑ์แอโรโซล อย่างไรก็ตามข้อมูลด้านการไหลภายในเอซีไอยังมีอยู่อย่างจำกัด รวมถึงจำเป็นต้องมีการสอบเทียบมาตรฐานที่ง่ายและเหมาะสมกว่าเดิม ดังนั้นเทคโนโลยีคอมพิวเตอร์จึงน่าจะมีประโยชน์และสามารถประยุกต์ใช้ในเอซีไอ

วัตถุประสงค์สำหรับการวิจัยนี้คือ เพื่อพัฒนาแบบจำลองพลศาสตร์การไหลด้วยคอมพิวเตอร์ในเครื่องเอซีไอและศึกษาผลของตัวแปรต่างๆ ในแบบจำลองที่มีการต่อพ่วงเครื่องมือด้วยอุปกรณ์คัดแยกอนุภาคขนาดใหญ่ นอกจากนี้ศึกษาการเคลื่อนที่และการกระจายตัวของอนุภาคภายในเครื่องเอซีไอทั้งการทดลองจริงในห้องปฏิบัติการและการสร้างแบบจำลองด้วยคอมพิวเตอร์

รวมถึงศึกษาความสัมพันธ์ระหว่างค่า Cut-off diameter ของแต่ละชั้นและค่ากลางของการกระจายขนาดอนุภาคที่อยู่บนแผ่นรองรับอนุภาคในเอซีไอจากล้องจุลทรรศน์และเครื่องมือวัดขนาดอนุภาคด้วยเลเซอร์

ผลการศึกษาพบว่า ค่าความเร็วอากาศผ่านรูเปิดภายในแต่ละชั้นของแบบจำลองพลศาสตร์การไหลในเอซีไอใกล้เคียงกับค่ามาตรฐานที่ได้มาจากโรงงาน (0.95, 1.75, 1.80, 2.94, 5.25, 12.72, 22.94 และ 45.49 เมตรต่อวินาที จากชั้น S0 ถึง S7 ตามลำดับ) สำหรับในชั้น S0 ถึงชั้น S7 มีค่าความคลาดเคลื่อนระหว่าง 1.59-8.10% พบว่าลักษณะการไหลของอากาศภายในแต่ละชั้นให้ค่าความเร็วของอากาศที่มีค่าสูงขึ้น จากจุดศูนย์กลางไปยังบริเวณด้านข้างของแผ่นรองรับอนุภาค และพบว่าอากาศมีความเร็วเพิ่มขึ้นจาก 1.13 เป็น 3.71 เมตรต่อวินาที และจาก 2.40 เป็น 8.68 เมตรต่อวินาที ภายในอุปกรณ์คัดแยกอนุภาคขนาดใหญ่ ที่อัตราการไหล 28.3 และ 60 ลิตรต่อนาที ตามลำดับ อย่างไรก็ตามความเค้นเฉือนภายใต้อุปกรณ์คัดแยกอนุภาคขนาดใหญ่มีผลต่อชั้นถัดมาคือมีความเค้นเฉือนราบเรียบมากกว่า เมื่อเทียบกับภายใต้อุปกรณ์ขาเข้ามาตรฐานในทั้งสองอัตราการไหลที่ใช้ในการทำงาน

นอกจากนี้จากการประเมินค่ากลางของขนาดอนุภาคที่อยู่บนแผ่นรองรับด้วยกล้องจุลทรรศน์ ได้ค่า 8.53 ถึง 0.92 ไมครอน ซึ่งสอดคล้องกับค่า Cut-off diameter จากบริษัทผู้ผลิตเอซีไอ (9.00 ถึง 0.40 ไมครอน) เช่นเดียวกับผลที่ได้จากเครื่องมือวัดขนาดอนุภาคด้วยเลเซอร์ โดยในชั้น S-1 ถึง ชั้น S3 ให้ค่าเปอร์เซ็นต์ความถูกต้องเข้าใกล้ 100% และเมื่อวิเคราะห์ขนาดอนุภาคของ silica microsphere บนแผ่นรองรับอนุภาค ด้วยเครื่อง Nanosizer ให้ค่า Z-average ในชั้น S4-S5 และตำแหน่งของพีคที่สูงสุดในชั้นที่ S6 ที่มีค่าใกล้เคียงกับค่ามาตรฐาน Cut-off diameter ที่ได้จากโรงงาน อีกทั้งการใช้แบบจำลองด้วยคอมพิวเตอร์โดยการใช้อนุภาคแบบขนาดเดียวให้ผล Cut-off

diameter สอดคล้องกับผลการทดลองจริง และแบบจำลองด้วยคอมพิวเตอร์โดยการใช้อนุภาคแบบหลายขนาดสามารถอธิบายการเปลี่ยนแปลงการกระจายของขนาดอนุภาคระหว่างเคลื่อนที่ภายในเอซีไอ โดยค่ากลางของขนาดอนุภาคลดลงตามขนาดของค่า Cut-off diameter ของแต่ละชั้นที่อนุภาคผ่าน

ดังนั้นจึงสามารถสรุปได้ว่า แบบจำลองพลศาสตร์การไหลสามารถอธิบายลักษณะการเคลื่อนที่ของอากาศภายในเครื่องเอซีไอตั้งแต่ทางเข้าไปจนถึงชั้นสุดท้าย ลักษณะการไหลของอากาศภายในอุปกรณ์คัดแยกอนุภาคขนาดใหญ่มีการเร่งความเร็วของอนุภาค และมีการเปลี่ยนทิศทางการไหลของอากาศ ซึ่งเป็นการยืนยันความสามารถของเอซีไอในการแยกอนุภาคขนาดใหญ่ออกจากกลุ่มอนุภาคตัวอย่าง และยังสร้างความเค้นเฉือนที่ราบเรียบบริเวณแผ่นรองรับอนุภาค ซึ่งสามารถลดการเกิดปรากฏการณ์ไหลกลับของอนุภาคที่อยู่บนแผ่นรองรับเข้าไปในกระแสลมอีกครั้ง ในส่วนของการสอบเทียบมาตรฐานเอซีไอนั้น ค่ากลางของขนาดอนุภาคและการกระจายของขนาดอนุภาคที่อยู่บนแผ่นรองรับอนุภาค มีค่าใกล้เคียงกับค่า Cut-off diameter และ Calibration curve ของแต่ละชั้นภายในเอซีไอได้เป็นอย่างดี นอกจากนี้ผลการจำลองด้วยคอมพิวเตอร์ได้แสดงการเคลื่อนที่ของอนุภาคภายในเอซีไอสามารถยืนยันและอธิบายผลการทดลองในห้องปฏิบัติการได้

Thesis Title The application of computational fluid dynamics in an Andersen cascade impactor for pharmaceutical aerosols

Author Janwit Dechraksa

Major Program Pharmaceutical Sciences

Academic Year 2015

ABSTRACT

Particle size distribution (PSD) is an important parameter to develop a pharmaceutical aerosol. An Andersen Cascade Impactor (ACI) is a standard device used to determine PSD traveling in the airstream, in which aerodynamic diameter is represented for PSD of the pharmaceutical formulation. Generally, the ACI operates within the designed condition for toxicology and pollution studies. There were various researches done in the pharmaceutical aerosol fields, mainly focused on the formulation development. The ACI becomes an interesting device. However, the fluid dynamic data in the ACI are still lacking, and the calibration process needs to be clarified for easier and more comfortable protocol to calibrate the ACI. Therefore, the computational technology could be a useful tool for pharmaceutical application.

The aims of this research work were to develop a validated computational fluid dynamic (CFD) model of the ACI and explore the effects of the add-on preseparator on the CFD parameters. The particle's traveling and distributing in the ACI were also investigated using both experimental and computational basis. The relationship between the cut-off diameter of each stage with the median size of particle size distribution (PSD) on individual collection plate via projected diameter and laser diffraction technique were studied.

The CFD model was validated by comparison with the manufacturer's nozzle velocity (0.95, 1.75,1.80, 2.94,5.25, 12.72, 22.94 and 45.49 m/s, from S0 to S7, respectively). For stage 0 to stage 5 of the ACI stages were found to be within a 3.56% error. CFD explored airflow in the whole ACI. The nozzle velocities were increased along the distance from the middle of the collection plate to the periphery. The flow field showed the airflow velocity accelerating by the preseparator at the induction tube from 1.13 to 3.71 m/s and 2.40 to 8.68 m/s (at 28.3 and 60 L/min of

flow rate, respectively). The preseparator produced smoother wall shear stress when compared to the ex-preseparator at both operational flow rates. PSDs on each collection plate were analyzed.

The microscopic size exhibited a gradient of particle size decreased at lower stages (8.53 to 0.92 μm). The laser diffraction technique showed the PSD of spray-dried mannitol correlated with the manufacturer's data at stage -1 to stage 3, which exhibited the percent relative accuracy (%RAC) close to 100% according to the median size of each preparation. The Z-averages of silica microsphere particles on the collection plate were comparable to the stage's cut-off diameter at stage 4 and stage 5. Peak's position had been chosen to link with the cut-off diameter at stage 6. The computational collection efficiency curves gave the simulated cut-off diameters close to the manufacturer's cut-off diameters using monodisperse tracking model. Furthermore, the polydisperse tracking model results could be used to explain the particle traveling. The 50% mass fractions of the simulated particle trapping were decreased in size along the lower stage of the ACI due to the reduced cut-off size of each stage.

In conclusion, the CFD explained total airflow started from inlet to the last stage of ACI. The airflow of the preseparator equipped model accelerated the airflow along the inlet port to maximize the trapping of desirable particles and generated a smooth wall shear stress at the collection plate to reduce the particle re-entrainment. The simulations also explained how the mono- and polydisperse particles traveled in the ACI as a calibrant. Moreover, the simulation of particle traveling along the ACI confirmed the calibration data. The median size and PSD of calibrant was a good representative for the stage cut-off diameter and calibration curve, respectively.

ACKNOWLEDGEMENT

The completion of a Ph.D. thesis work needs, a number of people's supports, and cooperation, which is very essential. A single person's effort is inadequate to complete this work without others support. Therefore, I would like to thank everybody who has been contributed to my thesis work either directly or indirectly. I am very much grateful to all of them.

First of all, I would like to express my deep and sincere gratitude to my mentor, **Associate Professor Dr. Teerapol Srichana**, Faculty of Pharmaceutical Sciences, Department of Pharmaceutical Technology, Dean of Graduate School, Prince of Songkla University, who has given me a golden opportunity to study Ph.D. program under his supervision. During my whole study period, his encouragement, proper guidance and support helped me to complete my work on time. His knowledge and logical way of thinking, hardworking and punctuality behavior inspired me as well as motivated me to work hard. I feel very lucky for having such a nice, cooperative and very helpful supervisor in every point of view. Words are insufficient to describe my appreciation and towards him.

I would like to extend my sincere thanks to Associate Professor Wibul Wongpoowarak and Associate Professor Dr. Damrongsak Faroongsarng, Faculty of Pharmaceutical Sciences, Prince of Songkla University, for their valuable advices to me during my proposal examination period. I extended my thanks to Dr. Kittinan Maliwan, Department of Mechanical Engineering, Faculty of Engineering, Prince of Songkla University who guided me in computational fluid dynamic theory.

I would like to thank Department of Pharmaceutical Technology, Faculty of Pharmaceutical Sciences, Prince of Songkla University, for providing me the facilities and providing all necessary supportive things during my Ph.D. tenure.

I also appreciated Drug Delivery System Excellence Center, Faculty of Pharmaceutical Sciences, Prince of Songkla University for providing all necessary facilities including printing of journals, thesis and other relevant papers to my thesis as well as scholarship throughout the study period. I humbly thank to all staff and scientists from this center (Ms. Wilaiporn Buatong, Mr. Ekawat Thawithong, Ms.

Kittiya Tinpun, Ms. Kornkamon Petyord and Ms. Titpawan Nakpheng) for their assistance and helpful advice for my thesis work.

I am also very much grateful to Dr. Brian Hodgson for editing my manuscripts.

I would like to thank my friends, Dr. Tan Suwandecha and Dr. Md. Iftekhar Ahmad, for their full support and co-operation for my Ph.D. thesis.

I would like to especially thank Ms. Panisara Boonsanong, education service officer of Faculty of Pharmaceutical Sciences, Prince of Songkla University, who has provided me all necessary information as well as papers required to complete the documents for official processes of Faculty of Pharmaceutical Sciences as well as Graduate School requirements.

Ultimately, I realize that this research work would not be happen without financial assistance, which was the vital thing for research work. Therefore, I would like to acknowledge a) Higher Education Research Promotion and National Research University Project of Thailand, Office of the Higher Education Commission; b) the Graduate School, Prince of Songkla University, c) Drug Delivery Excellent Center, Faculty of Pharmaceutical Sciences, Prince of Songkla University, d) Faculty of Pharmaceutical Sciences, Prince of Songkla University for providing financial support. This grant encompasses thesis fund, scholarship and conference fund for the whole study period.

Throughout my Ph.D. work, my beloved family stood with me in every ups and down and encourage me to bring out the best from me.

The author alone assumes responsibility for discussion and conclusions of this thesis and any errors of it may contain.

Lastly, the most special thanks go to all readers.

Janwit Dechraksa

CONTENTS

CONTENTS (Continued)

LIST OF TABLES

LIST OF TABLES (Continued)

LIST OF FIGURES

LIST OF FIGURES (Continued)

ABBREVIATION AND SYMBOLS

PSD	= Particle Size Distribution
ACI	= Andersen Cascade Impactor
CFD	= Computational Fluid Dynamic
m/s	= meter per Second
L/min	= liter per minute
%	= percent
μm	= micro meter
APSD	= Aerodynamic Particle Size Distribution
2D	= 2 dimensions
3D	= 3 dimensions
pMDI	= pressurized Metered-dose inhaler
DPI	= Dry powder inhaler
ACFM	= actual cubic feet per minute
mm	= millimeter
cm	= centimeter
W/2	= radius
Re	= Reynolds number
ρ	= density of air (kg/m)
u	= mean air velocity (m/s)
D	= characteristic linear dimension (diameter), nozzle diameter
μ_g	= dynamic viscosity of the fluid (Pa·s or N·s/m or kg/(m·s))
kg/m	= kilogram per cubic meter
Pa·s	= Pascal second
N·s/m	= Newton-second per square meter
Q	= flow rate
r	= nozzle radius
LRN	= low Reynolds number
Stk	= Stokes number
ρ_p	= density of particle
d_p	= particle diameter
$\vec{u}$	= air velocity vector
p	= air pressure
$\vec{\vec{\tau}}$	= stress, tensor
$\rho\vec{g}$	= gravitational body force
$\vec{F}$	= external body force
k_T	= turbulent kinetic energy
k_L	= laminar kinetic energy
ω	= the scale-determining variable
P_{k_T}	= production of turbulent kinetic energy by mean strain rate
R_{BP}	= bypass transition production term
R_{NAT}	= natural transition production term

ABBREVIATION AND SYMBOLS (Continued)

D_T = anisotropic (near-wall) dissipation for k_T
x_j = position vector
α_T = turbulent effective diffusivity
σ_k = kinetic energy turbulence constant
η = kinematic viscosity
$C_{\omega i}$ = turbulent viscosity coefficient
fw = damping function
f_ω = kinematic damping function
$F_D(u - u_p)$ = the drag force per unit particle mass
u_p = the particle velocity
F_x = an additional acceleration (force/unit particle mass) term
g_x = an additional gravitational force (force/unit particle mass) term
C_c = the Cunningham correction to Stokes' drag law
λ = the molecular mean free path
R = the ideal gas constant (8.314 J K^{-1} mol^{-1})
T = temperature (K)
N_a = the Avogadro's constant (6.023 x10^{23} mol^{-1})
°C = degree Celsius
kg/(m·s) = kilogram per meter-second
$\mathcal{T}_w$ = wall shear stress
$\mathcal{Y}$ = distance to the wall
V_p = volume of particle
V_{air} = volume of air
m_p = mass of particle
m_{air} = mass of air
$\acute{u}$ = turbulent velocity fluctuation
EIM = Eddy interaction model
UDF = User Defined Function
Ke = particle's kinetic energy
J = Joule
π = Pi
DE = deposition efficiency
Y_d = Rosin-Rammler distribution function
$\bar{d}_p$ = mean particle's diameter
n = spread parameter
l/h = liter per hour
ml/min = milliliter per minute
m^3/h = cubic meter per hour
SEM = scanning electron microscopy
keV = kiloelectron-volts
nm = nanometer
mg = milligram
g/l = gram per liter
min = minute

ABBREVIATION AND SYMBOLS (Continued)

cP	= centipoise
Z-average	= cumulant mean
PDI	= polydisperse index
µl	= microliter
µg/ml	= microgram per milliliter
r^2	= correlation coefficient
vs	= versus
ex-preseparator	= without preseparator
Pa	= Pascal
n	= number of sample
$Dv_{(0.5)}$	= volume median diameter
$Dv_{(0.9)}$	= volume diameter upper 90 percentile
$Dv_{(0.1)}$	= volume diameter lower 10 percentile
SE	= standard error
d_g	= geometric mean diameter
σ_g	= geometric standard deviation
d_{ln}	= length-number mean diameter
d'_g	= geometric mean diameter on weight basis
SN	= sonicated sample
nSN	= non-sonicated sample
Dv	= Inhaler device
Mi	= Metal inlet
Pre	= Preseparator
S-1	= Stage -1
S0	= Stage 0
S1	= Stage 1
S2	= Stage 2
S3	= Stage 3
S4	= Stage 4
S5	= Stage 5
S6	= Stage 6
RAC	= relative accuracy
GSD	= geometric standard deviation
LC	= liquid chromatography
RI	= refractive index
PIA	= particle in air measurement
PIL	= particle in liquid measurement

CHAPTER 1
INTRODUCTION

1.1 Rationale

The aerosol particle size is an important factor for many research works involved in the human respiratory system. The respiratory tract mainly has a function of exchanging carbon dioxide to red blood cell with oxygen from inhaled air. In the pharmaceutical science, the human respiratory tract could be used as a route of drug administration. A deposition pattern of particle in the respiratory tract is a key property of pharmaceutical aerosols. An aerodynamic particle size distribution (APSD) represents the actual size and size distribution of particle traveling in the air stream. It means that the APSD can be a parameter used to predict particle deposition in human airways. Cascade impactors have been developed to characterize the APSD and particle deposition, by fraction aerosols using aerodynamic diameter. The inertial impaction principle was used, where different aerodynamic size had shown different inertial force. The specific aerodynamic diameter had been collected on individual collection plate (Marple and Liu, 1974). Even though if cascade impactor was not a perfectly represented realistic respiratory tract, it attempted to compare the data between formulation and products (Mitchell et al., 2007).

The Andersen cascade impactor (ACI) is a conventional cascade impactor that has been used in various aerosol sciences (Li et al., 2013; Duan et al., 2014; Srichana et al., 2014). Each stage of the ACI is composed of a number of nozzles that are specifically designed, precisely built, and arranged radially. The nozzles gradually accelerate airstreams to a higher air velocity as the air flows through. The larger particles are retained on the earlier collection plates as the aerosols flow along the impactor. USP 39, <601> on Aerosol, recommends using a cascade impactor for the evaluation of pharmaceutical aerosols (United States Pharmacopeial Convention, 2015). According the design of ACI, there is various ways to modify the impactor by add-on stage or additional equipment on the top of the ACI, it has been more and more interested. Furthermore, there is modification in changing operation condition from normal operation flow rate (28.3 L/min) to higher

flow rate (60 L/min) or to lower flow rate (10-20 L/min) equipped with a mixing inlet (MIXINLET) (Nichols et al. 1998; Nadarassan et al. 2010). The published calibration method include fluorometric well-known calibration method, using methylene blue dye generated monodisperse and polystyrene latex, using monodisperse spherical silica powder, and pressure drop measurement call “in-use calibration” (Flesch et al. 1967; Rader et al. 1991; Srichana et al. 1998; Kwon et al. 2003; Nichols et al. 2013). However, time consuming and lacking of data linking between nozzles with pressure drop are the limitations of those calibration methods. Therefore, for the better understanding of the calibration technique, an alternative or complementary calibration method should be investigated. The next challenge for ACI studies is represented by the application of computer simulation to fluid flow and particle travelling in ACI. Computational fluid dynamic (CFD) is the tool for understanding and characterizing airflow in any aerosol science. There is many example of using CFD in pharmaceutical field. Gulak et al. simply used 2D CFD model to determine if gravity affected the deposition of the particles. The simulation result gave a good agreement with an experimental setup in the case of a single-nozzle impactor operated at 28.3 L/min (Gulak et al., 2009). There is also the 2D CFD study in add-on equipment in the ACI operating set to reveal the velocity with pressure profiles and the deposition regions in the preseparator (Sethuraman and Hickey 2001). Vinchurkar et al. (2009) described the effects of the aerosol charge using multiple-jet models (whole stage cascade impactor), which produced clear flow patterns, that were more useful when compared to a single jet design (Vinchurkar et al., 2009). CFD model can be used to predict or analyze fluid flow and particle travelling in ACI.

The objectives of this research were to develop a CFD model for the Mark II ACI and study the effect of fluid flow, airflow pattern and add-on equipment in ACI model. Monodisperse and polydisperse particle travelling were investigated in ACI by using experimental data and computational data. The fluid models of ACI were developed from available dimensional information. Introducing monodisperse and polydisperse aerosols were done into the real experimental and CFD model. Both experimental and computational data had been used to explore the fluid dynamics and particle travelling in the ACI.

1.2 The objectives of this study

1.2.1 To develop a computational fluid dynamic model for the Mark II Andersen cascade impactor

1.2.2 To validate the CFD model based on the numerically predicted characteristics of the Andersen cascade impactor and manufacturer's data.

1.2.3 To classify the flow field, airflow function, and the effect of the preseparator and ex-preseparator in the ACI model, by using the CFD study to simulate typical operational conditions

1.2.4 To validate the collection efficiency of the Andersen cascade impactor based on simulation and experimentation.

1.2.5 To develop polydisperse aerosols calibration method for impactor

1.2.6 To observe particle size distribution on each stage's collection plate

1.2.7 To confirm the calibration procedure using computer aided method

1.2.8 To investigate the accuracy of a polydisperse aerosols calibration method for impactor and calibration validation.

CHAPTER 2
LITERATURE REVIEWS

2.1 Pulmonary delivery

To treat respiratory diseases, pulmonary drug delivery is a preferred route of drug administration. It provides three main advantages. First, an immediate local effect with direct delivery to the target organ can be achieved, which allows for a decreased dosing. Second, the large surface area of the lung with high blood supply for relatively rapid drug absorption. Finally, the first pass metabolism could be avoided, resulting in increased the bioavailability of the drug (Moeller and Jorgensen, 2008). According to the lung anatomy, the continuing dividing of the airway from the trachea divides into two main bronchi to multiple divisions, gives rise to bronchioles. The bronchial tree continuously splits until the bronchiole level, which leads to the alveoli. Clusters of alveoli that are enormously composited in the human lung provide a large surface area. The individual alveoli are wrapped by capillaries, where gas and exchange of chemicals occur. Through this pathway, drug delivery systems can be effectively administered by the pulmonary route. Therefore, deoxygenated blood is driven through the pulmonary artery. The oxygen-rich blood is returned to the heart via the pulmonary veins to be pumped back into systemic circulation without first pass metabolism by the liver.

The inhaled air passes through the mouth or nose where particles of a size larger than 10 μm are trapped in the oropharynx, nasopharynx and larynx before it travels through the deeper respiratory tract. The particle sizes range from 2-10 μm will be deposited at the trachea or in the gradually subdividing system of bronchi and bronchioles depending on their size. Some of aerosol particles (less than 2 μm) can reach the terminal alveoli.

Generally, an inhaler is classified into three main types. The common type of inhaler is the pressurized metered-dose inhaler (pMDI). In pMDIs, medication is most commonly stored in solution/suspension and filled with a propellant in a pressurized canister as a driving gas. The pMDI canister is prescribed with a plastic

hand-operated actuator. Once triggering, the metered-dose inhaler releases an aerosol form of a fixed dose of medication. The second type of inhaler is a dry powder inhaler (DPI) that releases a dose of medicine as a powder aerosol. The medicated powder will be inhaled and disaggregated to micron size by the patient upon inhalation. Finally, nebulizers supply the medication as an aqueous formulation.

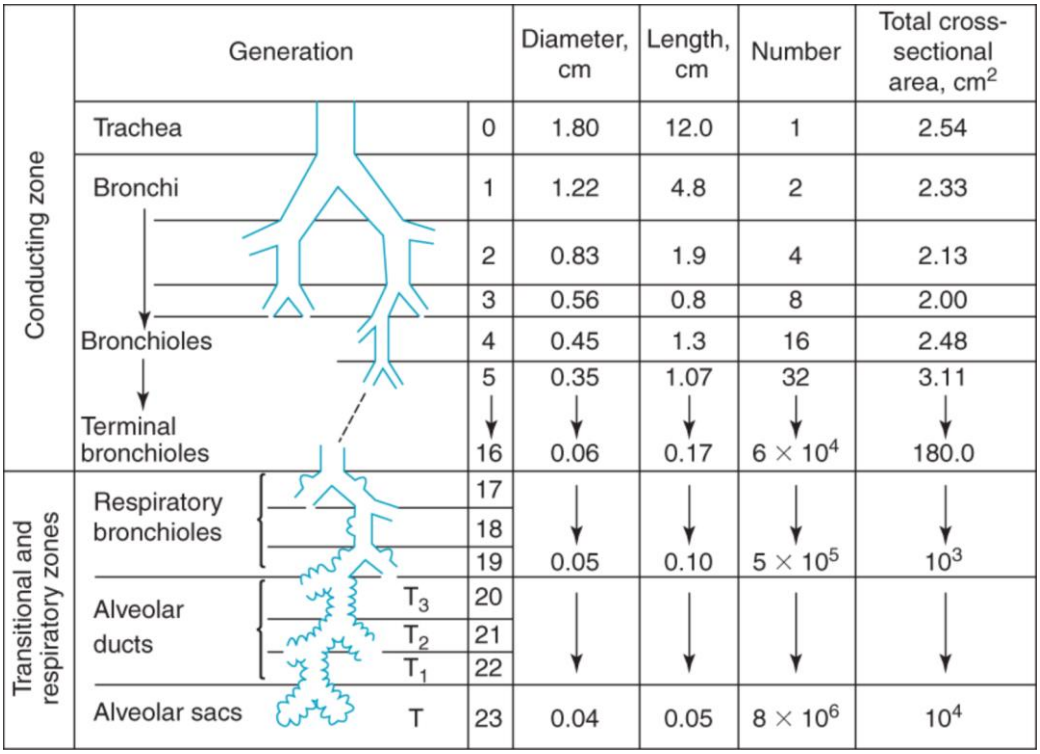

	Generation		Diameter, cm	Length, cm	Number	Total cross-sectional area, cm^2
Conducting zone	Trachea	0	1.80	12.0	1	2.54
	Bronchi	1	1.22	4.8	2	2.33
		2	0.83	1.9	4	2.13
		3	0.56	0.8	8	2.00
	Bronchioles	4	0.45	1.3	16	2.48
	Terminal bronchioles	5 ↓ 16	0.35 ↓ 0.06	1.07 ↓ 0.17	32 ↓ 6×10^4	3.11 ↓ 180.0
Transitional and respiratory zones	Respiratory bronchioles	17 18 19	↓ 0.05	↓ 0.10	↓ 5×10^5	↓ 10^3
	Alveolar ducts	T_3 20 T_2 21 T_1 22	↓	↓	↓	↓
	Alveolar sacs	T 23	0.04	0.05	8×10^6	10^4

Figure 1 Pulmonary drug delivery pathway and deposited particle size on each air region (Levitzky, 2013)

2.2 Andersen cascade impactor

It is very important to understand the airflow that carries drug particles for determination of the aerodynamic particle size and deposition in the lung. Cascade impactors are developed for aerosol particle sizing using theoretical and numerical studies of particle size and flow characteristics. According to US pharmacopeia, there are a variety of cascade impactors nowadays. These instruments are frequently employed to determine the aerodynamic mass-weight size distributions of aerosols from a variety of sources. Generally, uniformity of a delivery-dose over the entire content is required for inhalers (metered-dose inhaler or dry powder inhalers)

containing drug formulations, multiple doses of drug formulation and in reservoirs or pre-metered dosage units. The uniformity of the delivery-dose of an inhaler ensures that the delivered drug level is in the therapeutic range and provides identical doses. According to the US pharmacopeia, evaluations required other parameters than particle size; that include an aerodynamic size distribution, drug delivery efficiency and drug deposition sites. Particle size and aerodynamic size distribution can be characterized using a cascade impactor or other particle size measurement. The cascade impactor determines the size of aerosol particles by a multi stage jet collection plate wherein each stage allows different sizes to pass through. The impactor collects all particles larger than a certain size whilst smaller particles pass through the stage with the air stream (Marple and Willeke, 1976b; Marple and Willeke, 1976a; Liu, 2012). However, several impactor types are used to characterize particle properties based on the US pharmacopeia such as an ACI, multi-stage impinger, Marple-Miller impactor, etc., The ACI shows good agreement with clinical results and is in practice useful for evaluation of aerosols (Graseby-Andersen, 1985; Hassan and Lau, 2011).

The first design of the ACI is comprised of a glassware induction port or metal inlet, an optional impactor preseparator and nine stages (including a backup filter holder). Three-spring clamps hold all stages together and an o-ring seal cover between stages. A representative Mark II ACI is shown in Figure 2 including a preseparator and glassware induction port. The glassware induction port is tubular with a ball geometry and a turn of 90° that is used to direct aerosols from the inhalation devices into the preseparator and the impactor (United States Pharmacopeial Convention, 2015). Each impactor's stage consists of multiple jets that direct air and particles onto a collection plate. Each stage is an aerodynamic classifying sieve for the formulation of aerosols. The sampling device is used as a particle collector so that the device simulates the respiratory tract, so lung penetration by the aerosol particles can be predicted. Aerosols are trapped onto the collection plates by impaction as a function of their aerodynamic size. The characteristics of the jets have effects on the particles momentum. The preseparator is designed to capture several grams of oversized aerosol particles to prevent an overload of particles. The

particles in the preseparator should be carefully collected and analyzed separately or grouped with stage 0. The stage 0 is the upper stage of the impactor and is designed to capture particles greater than approximately 9.0 μm. The remaining stages have progressively smaller diameter jets, which result in higher velocities and the impaction of smaller aerodynamic particle size as shown in Figure 2.

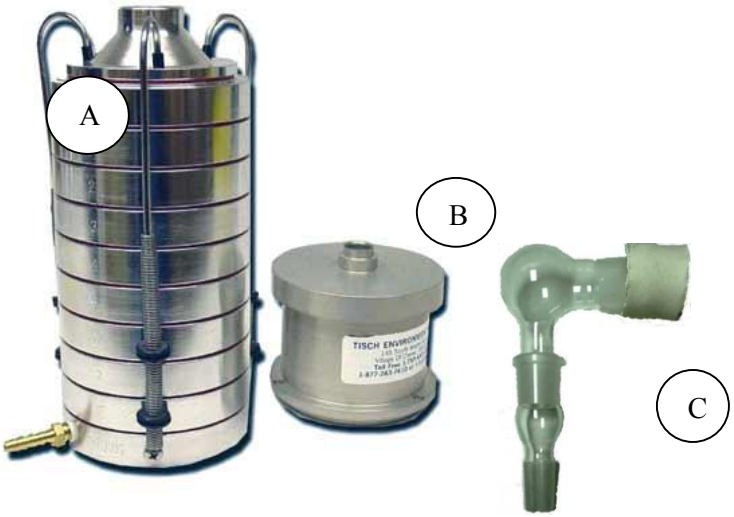

Figure 2 Eight stages Mark II Andersen cascade impactor (A), preseparator (B) and the glass throat (C) induction port

The ACI is the instrument of choice to characterize the particle size and to predict particle deposition patterns. The ACI has been generally designed to operate at 28.3 L/min of an inhalation flow rate (consisting of 8 stages) with recent applications to allow determinations at 60 and 90 L/min (adapted equipment stage) so that each flow rate provides a different cut-off diameter. For use of non-standard flows with the ACI, it needs to have the cut-off diameters for the stages recalculated. However, the recommended flow rate of the Pharmacopoeias is low to provide clinical relevance. An accurate determination of the size distribution for these aerosols is essential to forecast the available respiratory fraction. The result will define the site of deposition in the respiratory tract, absorption into the tissue and blood, and subsequent drug effectiveness or potential adverse effects. Obviously the methods used for evaluation of aerosol particle size and an understanding of particle deposition, must be very precise to provide accurate information on drug particle flow characteristics. Details of the individual ACI stages including the number of jets, jet

diameters and jet velocities at a flow rate of 28.3 L/min, or 1 actual cubic feet per minute (ACFM) by the manufacturer (Graseby-Andersen, 1985) are provided in Table 1. Additional parameters are characterized by the studies of Marple and Willeke (1976b) and Fang et al. (1991). As shown in Table 1, the number of jets per stage ranges from 96 to 400; stage 0 and 1 have 96 jets arranged in a radial pattern, there are 400 jets in stages 2-6; stage 7 contains 201 jets. Each stage connects to a collection plate, which is disk-shaped with a diameter of 8.255 cm, to receive an impact of the particles. The distance between the jet outlets and collection plates are 1.02 mm for stages 0 and 1, and 2.15 mm for the remaining stages. The use of multiple jets in the ACI allows for a high flow rate while maintaining laminar jet conditions. The diameters of the ACI jets vary from approximately 2.6 mm in stage 0 to 0.25 mm in stages 6 and 7. The constant flow rate and the smaller diameter jets increase the velocity of the sampled air in the lower stage. A key performance parameter for each specific impactor stage is the particle collection efficiency. Such a perfect efficiency curve would be appeared as a vertical straight line on a graph that expresses the collection efficiency against particle sizes. The greater efficiency curve is ideally S shaped with a sharper gradient that reflects the quality of the design of the impactor stage (cut-off point of that impactor).

Normally, the principle of particle sizing is based on the aerodynamic behavior of aerosol particles and inertial impaction (Figure 3). An aerosol is passed through a nozzle and the air stream is directed against a collection plate, where the particles strike and stick on. The plate deflects the flow to form an abrupt 90° bend in the streamline. While the direction of airflow changes, the aerosol particles continue to move on the original direction of flow until they lose inertia because of friction with molecules in the surrounding medium. These particles relax into the new direction of the airflow and the time for this is called the relaxation time. If the particles are large enough and have sufficient inertia, this relaxation time will be too long and the particles will impact on the collection plate. On the other hand, smaller particle will relax into the new direction. Therefore, particles larger than a selected aerodynamic diameter are removed from the airflow by impaction whilst those

smaller than the size continue to remain in the streamline. In fact, the particle size cut-off actually exists as a collection efficiency curve against particle size.

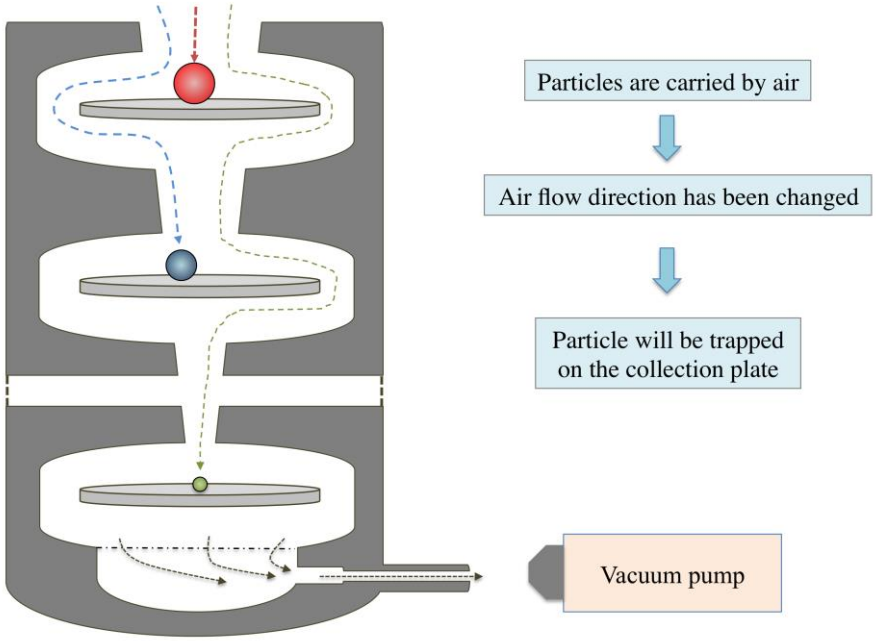

Figure 3 Impactor principle based on inertial impaction

ACI calibration

The US Pharmacopoeia (United States Pharmacopeial Convention, 2015) specifies the use of a cascade impactor for the measurement of the size distribution of aerosols; at a flow rate through the impactor sufficient to mimic inhalation and prevent backward trajectories when a test device, such as a metered dose inhaler is activated. Commercially available impactors such as the 8-stage ACI are usually operated at low flow rates (28.3 L/min). A flow rate at 60 L/min is the accepted standard for using in dry powder inhalers (United States Pharmacopeial Convention, 2015). More recently, it has been used at a flow rate as high as 60 L/min to comply with the USP flow rate specification (United States Pharmacopeial Convention, 2015). This practice is not recommended without a recalibration of the impactor.

Monodisperse aerosols were generated into specific particle size by vibrating orifice aerosol generator and introduced to the impactor. The deposition efficiency of each particle size was calculated as a ratio of mass collected on the stage to a total mass. The total mass of size aerosol was obtained by summation of all stages (Rader et al., 1991; Kwon et al., 2003). Srichana, et al. has first published the calibration method using spherical silica for the ACI. The monodisperse particle sizes were separately introduced to determine the collection efficiency curve of the preseparator, stage 0 to stage 4 (Srichana et al., 1998).

Also, there is an indirect calibration used as an alternative, which is called “in-use calibration”. The stage flow resistance (pressure drop) measurement could be used to determine the effective diameter of each stage, which is related to stage cut-off diameter. However, more data about nozzle discharge coefficient linking with pressure drop are needed to assess before this approach can be advocated (Nichols et al., 2013). The purpose of calibration and verifying the actual performance of the ACI is to validate the size cut-off of each stage in the impactor and to provide the quality control for the impactor.

2.3 Theoretical and Numerical studies

Theoretical and numerical studies have been conducted to evaluate the effects of the design and flow conditions on determination of the distributions and deposition of aerosol size. Several studies have focused on improving and characterizing the performance of impactors, as well as developing impactors for specific applications (Andersen, 1966; Cohen and Montan, 1967; Lundgren, 1967). As well as, the principles of impactor have been investigated using numerical studies (Marple et al., 1974; Marple and Liu, 1974; Marple and Willeke, 1976b; Barnocky and Davis, 1988). There was one study aimed to determine a numerical calibration of the ACI as a single jet simulation (Gulak et al., 2009; Abouali et al., 2011). However, it focused on the particle deposition at each stage in two-dimensions on a single jet asymmetry (Figure 4) by solving the Navier-Stokes equation. It was shown to be in good agreement with the available experimental data.

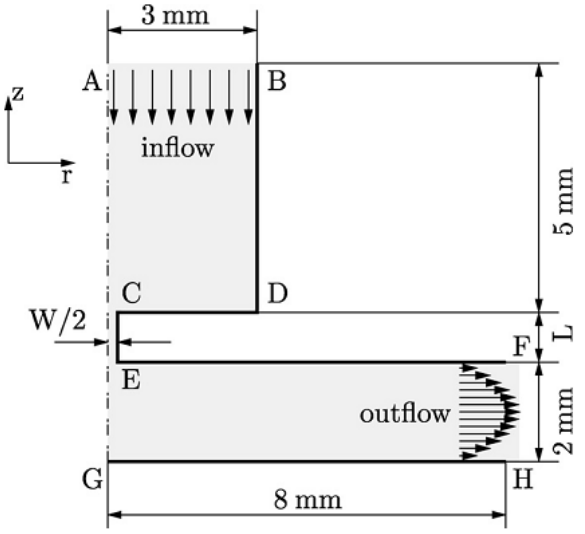

Figure 4 A schematic representation of the single stage model (Gulak et al., 2009)

A number of open questions remain. In the airflow field, unknowns include the degree of flow distribution among the jets of a single stage, the amount of flow recirculation, and airflow characteristics responsible for wall losses. Size changes of aerosols within the impactor due to hygroscopic growth or evaporation is also known to influence impactor performance (Longest and Vinchurkar, 2007).

Reynolds number

The Reynolds number, which is a ratio between the inertial and viscous forces, can be used to evaluate whether viscous or free flowing equations are appropriate to the problem. It can be interpreted that when the inertial forces dominate over the viscous forces (when the fluid is flowing faster and R_e is larger) then the flow is turbulent. When the viscous forces are dominant (slow flow, low R_e), they are sufficient to keep all the fluid particles in line, then the flow is laminar. The ranges of the Reynolds numbers based on the nozzle diameter are shown in equation 1.

$$Re = \frac{\rho u D}{\mu_g} \qquad \text{Equation 1}$$

Where u is the mean fluid velocity (SI unit: m/s); D is a characteristic linear dimension, (hydraulic diameter); μ is the dynamic viscosity of the fluid (Pa·s or N·s/m or kg/(m·s)); ρ is the density of the fluid (kg/m)

Flow rate equation

$$Q = u\pi r^2 \qquad \text{Equation 2}$$

where Q is a flow rate, u is the air velocity and r is the nozzle radius.

The ranges of Reynolds number used to characterize fluid flow regimes within similar fluid are as follow.

1. Laminar flow: where Re < 2000 there is a movement of flowing particles, with no disruption between layers. At low velocity, there is no lateral mixing.

2. Transitional flow: 2000 < Re < 4000 there is movement of flowing particles that are characterized by being between laminar and turbulent flow, the flowing particle has little disruption and does not cross over the flow line.

3. Turbulent flow: where Re > 4000, a common type of flow usually occurs at 'high' velocity of flow. The directions of flow are represented by average motion because particles in the fluid are completely irregular. Therefore, the mathematical analysis is very complex.

Based on these conditions, flow is assumed to be laminar or transitional in the preseparator and fully laminar in the impactor stages. To simulate conditions in the preseparator, the low Reynolds number (LRN) k–ω model is chosen based on its ability to accurately predict pressure drop, velocity profiles and shear stress for transitional and turbulent flows (Ghalichi et al., 1998;Wilcox, 1998).

Particle deposition

During the flow of particles along the cascade impactor, the collection plates at each stage will collect the loose particles free from inertia. There are three main airborne particle deposition mechanisms (diffusion, inertial impaction and sedimentation). Nonetheless, the particle sizing mechanism of the ACI is mainly described by inertial impaction. In general, each size range of particles are collected by the preseparator and the eight stages, depend on the velocity at the nozzle of each stage and distance between the nozzles and collection plate that is known as the “relaxation distance” to represent the impaction parameter.

Stokes number (Stk) is dimensionless parameter, which is defined by the ratio of the stopping distance and jet diameter that are shown in equation 3. The

stopping distance relates to particle properties (dimension, density and velocity) acted on specific fluid condition as shown in equation 4.

$$Stk\ number = \frac{stopping\ distance}{dimension\ of\ nozzle(diameter)} \quad \text{Equation 3}$$

$$Stk = \frac{\rho_p d_p^2 U}{9\mu_g D} \quad \text{Equation 4}$$

Where ρ_p (kgm^{-3}) is particle density, d_p is the particle diameter, U is the fluid velocity, μ_g is the gas viscosity and D is the nozzle's diameter

2.4 Computing and Related equations

The flow in the preseparator and ACI was considered as a steady, incompressible gas, and isothermal system under standard laboratory conditions. The conversion equations used in this study are shown below.

Conservation of mass $$\frac{\partial \rho}{\partial t} + \nabla \cdot (\rho \vec{u}) = 0 \quad \text{Equation 5}$$

Conservation of momentum $$\frac{\partial}{\partial t}(\rho \vec{u}) + \nabla \cdot (\rho \vec{u}\vec{u}) = -\nabla p + \nabla \cdot \left(\vec{\vec{\tau}}\right) + \rho \vec{g} + \vec{F} \quad \text{Equation 6}$$

Where $\vec{u}$ is the velocity vector, p is the pressure and ρ is the fluid density, $\vec{\vec{\tau}}$ is the stress, tensor and $\rho \vec{g}$ and $\vec{F}$ are the gravitational body force and external body force, respectively.

The Three-Equation Eddy Viscosity Model was selected as a transitional flow system using literature reviews, which gave the most stable and less use of computational power. The Three-Equation Eddy Viscosity Model ($k - k_L - \omega$) for transitional flows was employed for all CFD calculations (Walters and Cokljat, 2008).

$$\frac{Dk_T}{Dt} = P_{k_T} + R_{BP} + R_{NAT} - \omega k_T - D_T + \frac{\partial}{\partial x_j}\left[\left(\eta + \frac{\alpha_T}{\sigma_k}\right)\frac{\partial k_T}{\partial x_j}\right] \quad \text{Equation 7}$$

$$\frac{Dk_L}{Dt} = P_{k_L} - R_{BP} - R_{NAT} - D_T + \frac{\partial}{\partial x_j}\left[\eta \frac{\partial k_L}{\partial x_j}\right] \quad \text{Equation 8}$$

$$\frac{D\omega}{Dt} = C_{\omega 1}\frac{\omega}{k_T}P_{k_T} + \left(\frac{C_{\omega R}}{fw} - 1\right)\frac{\omega}{k_T}(R_{BP} + R_{NAT}) - C_{\omega 2}\omega^2 + C_{\omega 3}f_\omega \alpha_T fw^2\frac{\sqrt{k_T}}{d^3} + \frac{\partial}{\partial x_j}\left[\left(\eta + \frac{\alpha_T}{\sigma_\omega}\right)\frac{\partial \omega}{\partial x_j}\right] \quad \text{Equation 9}$$

Where, k_T is turbulent kinetic energy

k_L is laminar kinetic energy

ω is the scale-determining variable

P_{k_T} is production of turbulent kinetic energy by mean strain rate

R_{BP} is bypass transition production term

R_{NAT} is natural transition production term

D_T is anisotropic (near-wall) dissipation for k_T

x_j is position vector

α_T is turbulent effective diffusivity

σ_k is kinetic energy turbulence constant

η is kinematic viscosity

$C_{\omega i}$ is turbulent viscosity coefficient

fw is damping function

f_ω is kinematic damping function

Equation 10 describes particle travelling in the air stream.

$$\frac{dv_p}{dt} = F_D(u - u_p) + \frac{g_x(\rho_p - \rho)}{\rho_p} + F_x \quad \text{Equation 10}$$

Where, $F_D(u - u_p)$ is the drag force per unit particle mass

u is the mean air velocity

u_p is the particle velocity

F_x is an additional acceleration (force/unit particle mass) term

According to equation 10, drag force of particle depends on particle's diameter, density and fluid viscosity as equation 11. In addition, the Cunningham slip correction factor is used to account for non-continuum effects when calculating the drag on small particles.

$$F_D = \frac{18\mu_g}{{d_p}^2 \rho_p C_c} \quad \text{Equation 11}$$

$$C_c = 1 + \frac{2\lambda}{d_p}\left(1.257 + 0.4e^{-\left(1.1d_p/2\lambda\right)}\right) \quad \text{Equation 12}$$

$$\lambda = \frac{RT}{\sqrt{2}\pi d N_a P} \quad \text{Equation 13}$$

Where, μ_g is the molecular viscosity of the fluid

d_p is the particle diameter

ρ_p is the particle density

C_c is the Cunningham correction to Stokes' law

λ is the molecular mean free path

R is the ideal gas constant (8.314 J K^{-1} mol^{-1})

T is the temperature (K)

N_a is the Avogadro's constant (6.023 x10^{23} mol^{-1})

All information of ACI could be applied to fulfill the computational simulation model. The full fluid dynamics in the ACI is still interested. The modified operation condition should be studied to explore the effect of adding preseparator in airflow pattern and velocity. The ACI calibration method for dry powder basis could be studied by introducing monodisperse and polydisperse into ACI based on both experimental and computational model. The calibrant preparation could be produced the appropriate particle's properties to use as a routine calibrant. The spray-dried technique has been selected to use in calibrant preparation because it directly relates to dry power inhaler preparation. Particle travelling path and PSD along ACI also could be computed using CFD and confirmed by experimental data. The simulated particle trapping result could be used to confirm calibration result that had obtained by experimental data.

CHAPTER 3
MATERIALS AND METHODS

3.1 Materials used in this study

Isopropyl alcohol, ethanol and methanol were obtained from RCI Labscan co. Ltd, Thailand. Mannitol powder was purchased from Sigma-Aldrich, St. Louis, USA. Three size of monodisperse silica microsphere were obtained from Cospheric LLC, Santa Barbara, CA USA.

3.2 Equipments and Instruments

Spray dryer Buchi B-290; BÜCHI Labortechnik AG, Flawil, Switzerland.
Nano Spray dryer Buchi B90; BÜCHI Labortechnik AG, Flawil, Switzerland.
Mastersizer dry cell, Mastersizer 2000 coupled to a Scirocco 2000 dry dispersion unit; Malvern Instruments, Worcestershire, UK
Mastersizer small cell, Mastersizer 2000; Malvern Instruments, Worcestershire, UK
Nano sizer, Zetasizer, NanoZS; Malvern, UK
Laser diffraction, Spraytec; Malvern Instruments Inc., Southborough, MA
Light Microscope; Olympus BH-2, Japan
Andersen cascade impactor (S0-S7,S-1-S6) +preseparator, ACI; Copley Scientific Limited, Nottingham, UK
HPLC with RI detector, Model RID-10A; Shimadzu, Kyoto, Japan

3.3 General modeling of ACI and model construction

A simple digital model of the ACI was created using the ANSYS FLUENT 13.0 (Figure 5). The geometric dimensions of ACI, number of nozzle, nozzle length and diameter (specific for each stage) were taken from the manufacturer (Graseby-Andersen, 1985) and measurements using a Vernier caliper (Table 1). Fluid parts were measured as discrete volumes. All fluid parts were first fused together from the preseparator to the filter stage of the fluid part. Reducing the multipart geometric dimension to a simpler geometry minimized the complexity of the ACI

model. The reducing complexity of the ACI was done by disregarding curvature (Vinchurkar et al., 2009). There are 2 sets of computational geometry. First, 28.3 L/min set was composed of stage 0 to stage 7 and the second is 60 L/min set that composed of stage -1 to stage 6. Both computational geometries of the ACI were connected to the preseparator.

Initially, models were constructed stage by stage until the full cascade impactor. As the complexity of the model was considered, the size of the model was reduced to optimize the computational resource. Stage division was applied to overcome that limitation. The 120° trisecting was the appropriate symmetry plane of the ACI model (Flynn et al., 2015).

Figure 6 shows the example of 120° trisecting on the ACI's stage 2. The divisions were applied on collection plate base's knobs, which has totally 3 position fitted with the divisions protocol.

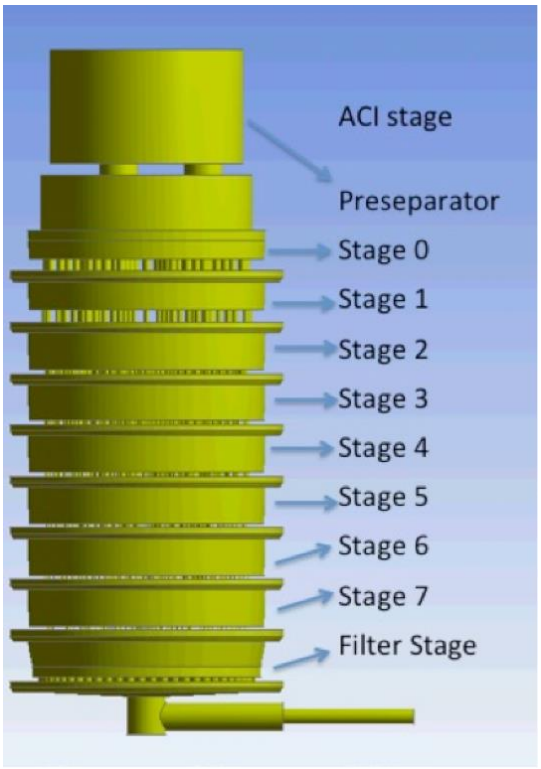

Figure 5 Andersen cascade impactor's fluid geometry of stage 0 to stage 7, preseparator and filter stage

Table 1 Andersen cascade impactor's specification on each stage: Number of nozzle, Nozzle's diameter, Nozzle's area, and calculated nozzle's velocity and Reynolds number of each nozzle (fluid flow) at specific condition (25 °C, 1.983×10^{-5} kg/(m·s) is the dynamic viscosity of the air and 1.1839 kg/m^3 is the density of air).

Stage	No. of nozzle	Nozzle's Diameter (mm)	Nozzle's area (m^2)	Total Nozzle's area (m^2)	28.3 L/min		60 L/min	
					Nozzle's velocity (m/s)	Re	Nozzle's velocity (m/s)	Re
-1	96	4.5	1.59E-05	1.53E-03			0.65	175.96
0	96	2.55	5.11E-06	4.90E-04	0.96	146.46	2.04	310.52
1	400	1.88	2.78E-06	2.66E-04	1.77	198.66	3.75	421.19
2	400	0.914	6.56E-07	2.62E-04	1.80	98.07	3.81	207.92
3	400	0.711	3.97E-07	1.59E-04	2.97	126.07	6.30	267.28
4	400	0.533	2.23E-07	8.92E-05	5.28	168.17	11.20	356.55
5	400	0.345	9.35E-08	3.74E-05	12.61	259.81	26.74	550.84
6	400	0.254	5.07E-08	2.03E-05	23.27	352.89	49.34	748.18
7	201	0.254	5.07E-08	1.02E-05	46.31	702.28		

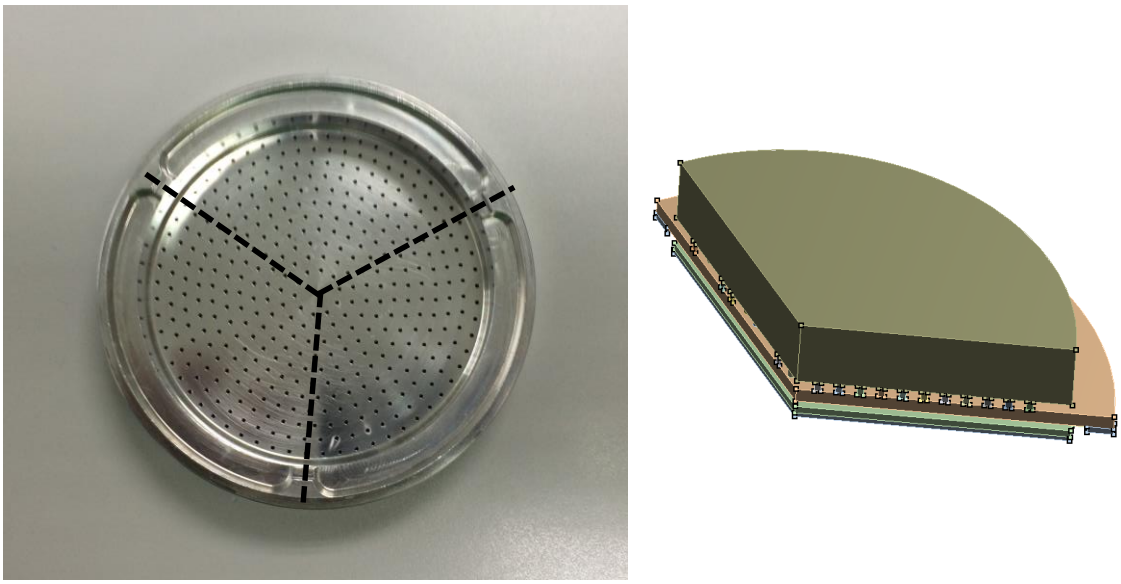

Figure 6 Division by 120° trisecting on stage (Example of stage 2)

3.4 Model meshing

ANSYS 13.0 meshing algorithm was used to develop two different meshing techniques as shown in Table 2.

Table 2 Meshing detail for computational geometries using ANSYS 13.0

Subject	Mesh A	Mesh B
Meshing Algorithm	hybrid unstructured hexahedral mesh with central axis of tetrahedral elements	Cartesian cut cell meshing
Purpose	Preliminary meshing	Final meshing

Mesh A was produced as a hybrid unstructured hexahedral mesh with central axis of tetrahedral elements, and Mesh B was produced as structured hexahedral mesh created by the Cartesian cut cell meshing algorithm. The meshing details were described in the Table 2 and Figure 7.

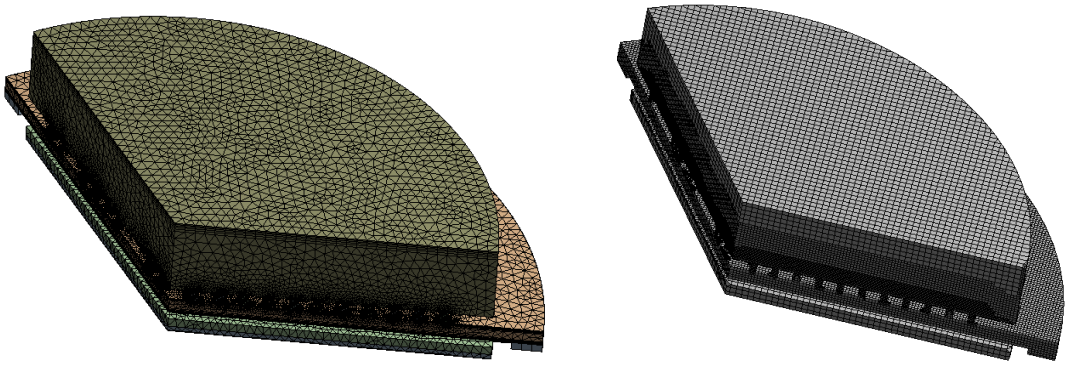

Mesh A Mesh B

Figure 7 Mesh configuration in model stage 2: Mesh A (Hybrid meshing) and Mesh B (Cartesian cut cell meshing)

3.4.1 Hybrid meshing

The volumes were meshed individually by different element shape was applied to appropriate geometry of the volume. Such Nozzles had been developed by sweep meshing algorithm with hexahedral mesh. While the stage body connected to other volume was meshed by multiple zone meshing algorithm of hybrid unstructured hexahedral together with central axis of tetrahedral elements. The connected geometry was meshed using Meshing 13.0 (Ansys Inc., USA) for the nozzle's velocity validation of 28.3 L/min. The hybrid unstructured hexahedral mesh with a central axis of tetrahedral elements were meshed for the complex model in the ACI and hexahedral mesh was used for the area near the nozzles.

3.4.2 Cartesian cut cell meshing

The fluid volumes of each stage (stage body, nozzles and collection chamber) were reunited using Boolean operations to form a single body before cut cell meshing had been done. The hard face sizing was applied to collection plate regions. The cell size over the post nozzle area was reduced when compared with inlet face's size to give continuity for particle trajectories. There were configurations for each stage meshing as shown in Table 3.

Table 3. Meshing configuration for each part of computational model

Setting configurations	Set to			
	S-1, S0, S1	S2, S3	S4, S5	S6, S7
Solver preference	Fluent	Fluent	Fluent	Fluent
Relevance	20	20	36	100
Relevance center	Fine	Fine	Fine	Fine
Smoothing	High	High	High	High
Cut cell feature Capture	15.0°	15.0°	15.0°	20.0°
Nozzle face sizing (mm)	Use program optimization	S2: 0.080 S3: 0.060	S4: 0.0761 S5: 0.0691	0.0822
Collection plate sizing (mm)	0.300	0.232	0.232	0.232
Inlet face sizing (mm)	0.4	1.0	0.8	1.0

3.5 Simulation conditions and Fluid flow parameters examination

For the first simulation, flow rate of 28.3 L/min, the maximum Reynolds number in the preseparator body was approximately to be 0.1057, and this indicated that laminar flow and Cunningham slip correction were incorporated in the simulation flow pattern in the cascade impactor (Dechraksa et al., 2014). To simulate the airflow and characterize particle trapped, laminar and transitional flow had been performed in the computational model.

To ensure that the flow pattern was correctly modelled, both an examination of the iterative convergence and experimental data were used to validate the computational model. First, the global mass and residual momentum was set as being lower than three orders of magnitude of the convergence of the flow field solution. Second, the predicted flow velocity at the nozzle of each stage was

compared with the characteristics of the Mark II ACI based on the manufacturer's data.

The characteristics of the wall shear stress at the collection plate were obtained under 2 inlet conditions (traditional and add-on preseparator). The wall shear stress can be explained by equation 14, where μ is the dynamic viscosity, $\mathcal{U}$ is the flow velocity parallel to the wall and $\mathcal{Y}$ is the distance to the wall.

Wall shear stress ($\mathcal{T}_w$)

$$\mathcal{T}_w = \mu \left(\frac{\partial \mathcal{U}}{\partial \mathcal{Y}}\right)_{\mathcal{Y}=0} \qquad \text{Equation 14}$$

To examine the fluid flow field in the full 3D preseparator, the velocity streamline, contour and vector were set to determine the direction of the flow characteristics in the interested model (preseparator and stage 0). Moreover, the velocity of each nozzle was characterized by average volume velocity at the nozzle's volume. The probe was used at a random position for determining the inlet velocity under the preseparator and ex-preseparator model.

3.6 Discrete phase model

3.6.1 Model description

The particle tracking employed discrete phase simulation of Fluent by Lagrangian discrete phase model based on as a one-way coupling. The discrete phase simulation was based on assumption that the discrete phase occupied a low volume fraction ($V_p << V_{air}$) and high mass loading ($m_p \geq m_{air}$).

The initial particle condition and initial velocity were specified as a constant and full turbulent profile, no slip condition were applied at the wall (Worth Longest and Vinchurkar, 2007). The injected particle was entrained into the air passing through each stage as shown in equation 7. The spherical particle model was employed for the particle injection greater than 1 μm. The particles range from 0.1-0.9 μm was fitted with Stokes-Cunningham model, which was taken into account the slip correction factor.

To mimic the real situation as particles were travelling in the air, the stochastic tracking approach had been used to predict the turbulent dispersion of the particle.

$$u_p = u + \acute{u} \quad \text{Equation 15}$$

Where, u is the mean air velocity

u_p is the particle velocity

$\acute{u}$ is the turbulent velocity fluctuation

3.6.2 Impaction parameter

Inertial force should be higher than continuous phase viscosity. Eddy interaction model (EIM) was used to describe the particle tracking into turbulent flow. The single particle is interacted with specific lifetime of eddy, after time over the particle completely crossed the interacted eddy. At that time, a new interaction between the particle and new eddy started (Matida et al., 2004).

3.6.3 Particle deposition simulation

In this study, particle deposition efficiency of each stage was calculated by number of particles that were trapped on the collection plate divided by number of particle entering into each stage. It depended on number of cell on the inlet surface of each model and the PSD from outlet of upper stage model were used for an inlet of the next stage model calculation.

3.6.4 Particle kinetic energy

Kinetic energy had been employed in particle trapping on the collection plate. Due to normal trap boundary condition, it expressed the under estimation of collection plate cut-off diameter. Therefore, the User Defined Function (UDF) had been developed by the following kinetic equations (equations 16-18). Particle density for silica is 1.8 g/ml and for mannitol is 1.5 g/ml.

$$Ke = \frac{1}{2} m_p \times {u_p}^2 \quad \text{Equation 16}$$

$$Mass = Volume \times Density \quad \text{Equation 17}$$

$$Volume\ of\ sphere = \frac{4}{3}\pi r^3 \qquad \text{Equation 18}$$

Where, Ke is particle's kinetic energy

m_p is the mass of particle in kilogram

u_p is the particle's velocity in meter per second

Deposition factor is the total deposition within the stage of interest can be explained by Lagrangian model by the number of discrete particles that deposit on the collection plate. The deposition efficiency (DE) was explained in equation 19.

$$DE = \frac{number\ of\ particle\ depositing\ in\ the\ region}{number\ of\ particles\ entering\ the\ region} \qquad \text{Equation 19}$$

Table 4 Calculated kinetic energy introduced to collection plate as a boundary condition

Stage	Cut-off in μm	Particle mass (kg)		K_e (J)	
		Silica	Mannitol	Silica	Mannitol
-1	9	6.87E-13	5.73E-13	1.47E-13	1.23E-13
0	5.8	1.84E-13	1.53E-13	3.83E-13	3.19E-13
1	4.7	9.79E-14	8.15E-14	6.89E-13	5.74E-13
2	3.3	3.39E-14	2.82E-14	2.46E-13	2.05E-13
3	2.1	8.73E-15	7.27E-15	1.73E-13	1.44E-13
4	1.1	1.25E-15	1.05E-15	7.87E-14	6.56E-14
5	0.7	3.23E-16	2.69E-16	1.16E-13	9.63E-14
6	0.4	6.03E-17	5.03E-17	7.34E-14	6.12E-14

3.6.5 Particle distribution model for group of particle tracking

PSD was expressed as Rosin-Rammler Diameter Distribution Method. The Rosin-Rammler distribution function (Y_d) is based on the assumption that an exponential relationship existing between the droplet diameter (Bailey et al., 1983), d, and the mass fraction of droplets with a diameter greater than d,

In this case, 2.071 was set for spread parameter, maximum diameter is 8.71 μm while minimum diameter is 0.21 μm and mean diameter of Rosin-Rammler

function is 3.36 μm with 28 particle size range. Trajectory sample histograms had been used to describe the particle distributions on each collection plate and outlet of each stage. Diameter of particle was set as a variable interest.

$$Y_d = e^{-(d_p/\bar{d}_p)^n} \quad \text{Equation 20}$$

Where, $\bar{d}_p$ is the mean diameter

d_p is the particle diameter

n is the spread parameter

3.7 Calibrant preparation

Spray-dried mannitol particles were used as calibrant. Polydisperse particles were obtained by spray drying the mannitol solution using mini spray dryer with high-performance cyclone and Nanospray dryer under different conditions as shown in Table 5.

The monodisperse silica microspheres (0.261, 0.690, and 1.18 μm) were first characterized by SEM technique and dispersed in methanol and HFA-134a to make a pressurized suspension (100mg/ml).

Table 5 Preparation conditions for spray-dried mannitol

Conditions	Atomization air (l/h)	Inlet Temp. (°C)	% Mannitol	Feed rate (ml/min)	Aspirator (m^3/h)
A	742	100	10%	3	35
B	742	150	2%	3	35
C	Vibrating cell	100	10%	Level 1	8.4
D	357	130	10%	3	35

3.8 Particle characterization

3.8.1 Scanning electron microscopy (SEM)

Powder morphology (monodisperse microsphere silica and spray-dried mannitol particle) was investigated using scanning electron microscopy (SEM-Quanta, Quanta 400; FEI, Tokyo, Japan) at 10 keV. Samples were mounted on carbon

double adhesive tapes and gold-coated (20 nm thickness) before imaging (Edwards Sputter Coater, UK).

3.8.2 Particle size measurement by Master sizer dry cell

The laser diffraction using Mastersizer 2000 with dry powder feeder (Scirocco 2000, Malvern, UK) was used for determination of particle size distributions of the spray-dried mannitol powders. Approximately 4 mg of spray-dried mannitol powder was dispersed in air using 4-bar pressure. A refractive index of 1.520 was used for spray-dried mannitol. Each sample was analyzed in triplicates. The focal length of the lens was 63 mm with active beam length of 40 nm. The particle size result was accepted when the obscuration was 10 %.

3.8.3 Particle size measurement by small cell Master sizer

The laser scattering using Master sizer S with small cell unit (Malvern, UK) was used to determine particle size distributions after deposition on the impactor stage. The saturated methanol with measured material was used to collect ten runs of particles. Then all suspended particles were measured. Second, the collected mannitol particles were gently removed from collection plate until about 20 mg mannitol obtained.

3.8.4 Particle size measurement by Nano sizer

The monodisperse silica particles on the last three stages (S4-S6) were rinsed with methanol and collected separately. Dynamic light scattering measurements were performed at the scattering angle of 173° (backscattering detection) using a Malvern Zetasizer Nano ZS. The trapped particles on stage 4 to stage 6 were suspended in the methanol and diluted up to a concentration of 0.05g/l. The particles were allowed to equilibrate at 25 °C into 4 side clear glass cuvette for 2 min. Three measurements were performed for a sample, each consists of 10 individual runs. The viscosity and refractive index of dispersant were 0.5476 cP and 1.326, respectively. For the silica particles, the refractive index and absorption were used to calculate volume and number size distributions (1.458 and 0.001, respectively). Those values were added to calculate the data. The PSD of different techniques were

compared using cumulative mean (Z-average size), polydispersibility index (PDI) and peak mean.

3.8.5 Particle size measurement by Spraytec®

The Malvern Spraytec® with inhalation cell had been used to define PSD. The Spraytec® equipped with a USP throat that had been used in place of the inhalation cell as shown in Figure 8. The equipment was connected directly to a particle-collecting filter and vacuum pump. The flow rate was set to 60 L/min in the measurement zone. The setting of 2 % obscuration was a trigger for all the measurements.

3.8.6 Mannitol assay

For the mannitol assay, spray-dried mannitol was analyzed using high performance liquid chromatography (HPLC) (Model LC-20; Shimadzu, Kyoto, Japan). A resolve C-18 column, 5 μm, 150 mm × 3.9 mm (Waters, Milford, MA, USA) was used as stationary phase with de-ionized water as mobile phase. Settings were as follow: flow rate 1 mL/min; injection volume 100 mL; retention time of 4 min. A refractive index detector (Model RID-10A; Shimadzu, Kyoto, Japan) was used. A calibration curve was constructed using standard solutions of mannitol from 10 to 400 μg/mL (r^2 = 1.000) (Adi et al., 2010).

Figure 8 Spraytec® unit with inhalation cell assembly used for PSD determination (Malvern, 2007)

CHAPTER 4
RESULTS AND DISCUSSION

4.1 Final geometries and Meshing of the ACI

The multi-stage nature of the ACI is a major puzzle, since it has complex geometrical information. The nozzle's dimension is 2000 fold less than stage's body (Gulak et al., 2009). Fluid parts were first discretised model's volume together from preseparator to filter stage of fluid part (Figure 5). The complexity of the ACI model was minimized by reducing geometric dimension complex, growth rate from cell to cell set as 1.2 together with a coarse meshing model. The preseparator's fluid part and the meshing of inlet model were obtained (Figure 9 and Figure 10).

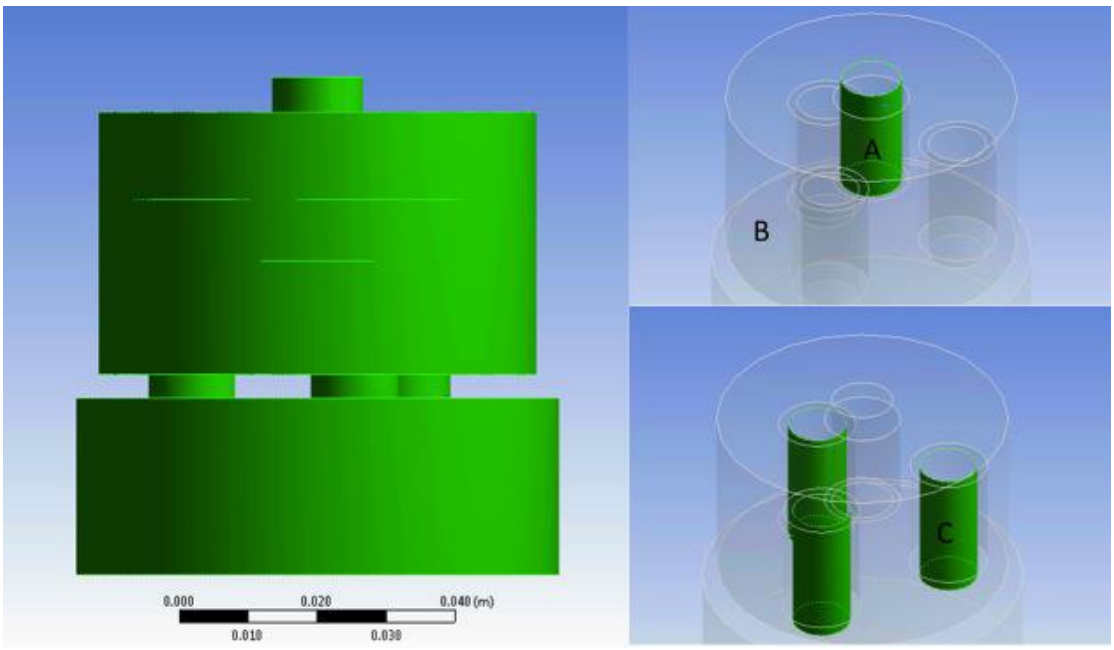

Figure 9 Geometry of preseparator: induction tube (A), middle plate (B), and connection tube (C).

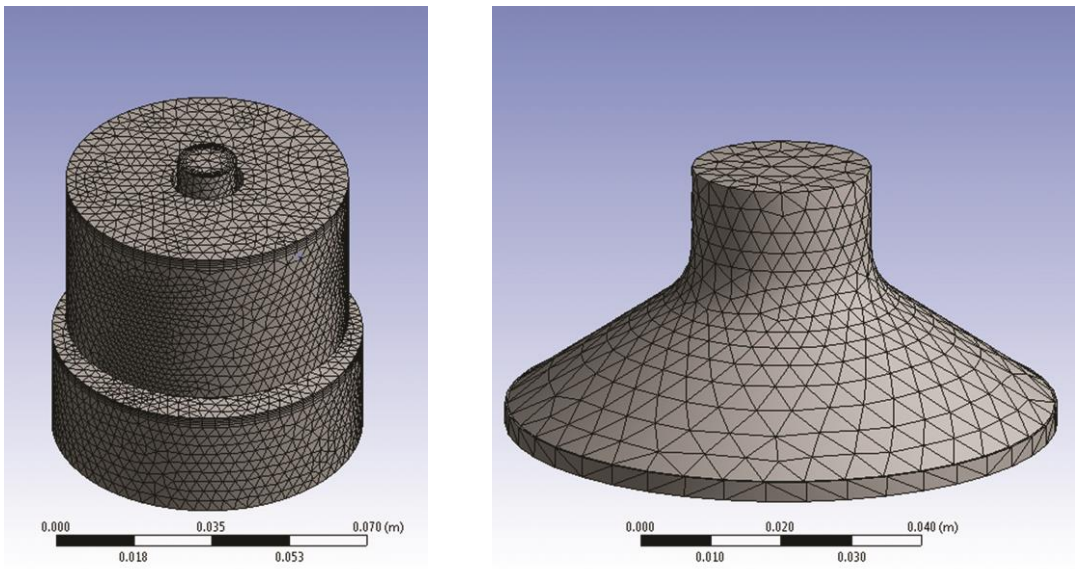

a) Preseparator b) Traditional USP metal inlet

Figure 10 Meshing of Preseparator (A) and traditional USP metal inlet (B)

4.2 Fluid phase flow simulation

4.2.1 Numerical validation

The airflow rate at 28.3 L/min was simulated for specific stages model to compare with manufacturer's data to examine experimental-simulation correlation. Based on the results (Table 6), the numerically predicted average nozzle velocities were comparable to the manufacturer's data.

Table 6. Numerical predictions of average nozzle velocities in meter per second compared with the manufacturer's data (28.3L/min) (Graseby-Andersen, 1985).

Stage No	0	1	2	3	4	5	6	7
Predicted nozzle velocity	0.98	1.73	1.75	2.99	5.39	13.10	24.80	48.70
Manufacturers' nozzle velocity	0.95	1.75	1.80	2.94	5.25	12.72	22.94	45.49
% Error for CFD vs. Manufacturer	3.56	1.59	2.78	1.73	2.74	2.98	8.10	7.05

As described, these average nozzle's velocity values were based on the summation velocities of each frame of the nozzle and divided by the number of frames at each stage. According to the manufacturer's data (Graseby-Andersen, 1985), numerical predictions were within approximately 3.56 % error for all stages except stage 6 and 7. In these later stages, the errors were within 8.10 % of the manufacturer's data. The increase in the % error of the predicted nozzle velocities at Stage 6 and 7 might be explained by considering the expected numerical inaccuracies, which for the other stages appear to be 3.56 % or less when compared to the manufacturers' data, and the significant increase in the solution complex associated with the decrease of the size of the nozzles from 0.127 mm (Sethuraman and Hickey, 2001). However, it confirms that how accurate the airflow pattern in cascade impactor by our boundary condition (Sethuraman and Hickey, 2001; Vinchurkar et al., 2009). In addition, the Reynolds's number of each stages were also comparable with these given nozzles velocity.

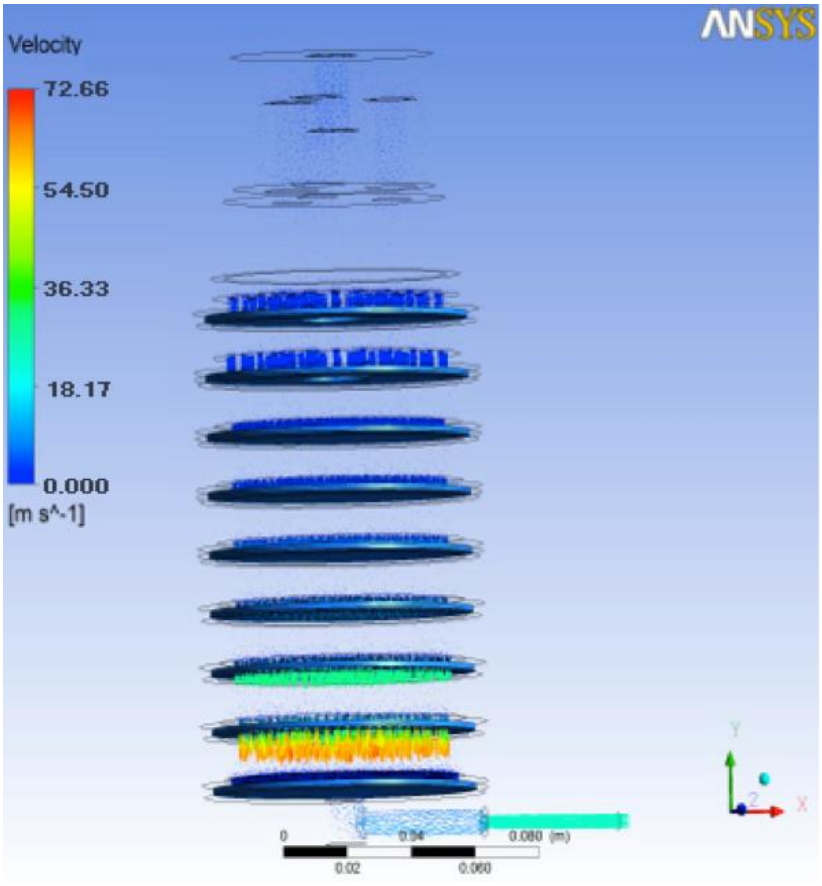

Figure 11 Velocity profile of whole ACI simulation

4.2.2 Velocity Profile

The velocity profile in Figure 11 presents the velocity (speed profile) at each nozzle location of the eight stages. The velocity increased steadily from stage 0 to stage 7 and the difference in velocity between stage 0 and stage 7 was greater than 70 %. The narrower space compressed the air traveling and resulting in the higher velocity (Gulak et al., 2009). The increasing nozzle velocity was capable to accelerate the particle velocity, and this shows good agreement with the acceleration of velocity of the particles (Morsi and Alexander, 1972). The increased particle velocity elevates the particle inertial force and promotes the impaction of the particles on the collection plate. It means that the small particles are likely to deposit at the lower stage because of the increasing air-particle acceleration produced by the narrowing diameter of the nozzles. The deposition of aerosol particles can be described by the equation 4.

4.2.3 Streamline field conditions of the preseparator

The three-dimensional streamlines (Figure 12) show that the velocity started from the preseparator to the lower stages. In the preseparator, the flow direction was observed to bend to the connection holes that passed the flow to stage 0. As the airflow was drawn through the connection holes, the bending zone of the airflow turns up to 360° where it started from the induction tube (A) straight to the middle plate (B) then turned 90° against the B plate. Then a 90-degree turn was again made when the flow hit the preseparator wall. At this point, the magnitude of the velocity decreased with the distance from the induction tube and was close to zero at the middle of the plate. This may increase the deposition on the preseparator wall of the large aerosol particles. The particle size, which was larger than 10 μm, lost their inertial force and deposited on the preseparator plate and wall (Sethuraman and Hickey 2001). Finally, the streamline was twisted sharply by about 180° because of the drawing force of the connection tube (C). By this process, the impactor reduced the particle load on stage 0 (and lower stages) and improved the particle-sizing ability. In this 3D model, the airflow pattern in the preseparator showed some disagreement from the 2D model where the streamline was drawn directly to the

connection tube (C) because of the limitations of the geometrical model's dimensions (Sethuraman and Hickey, 2001).

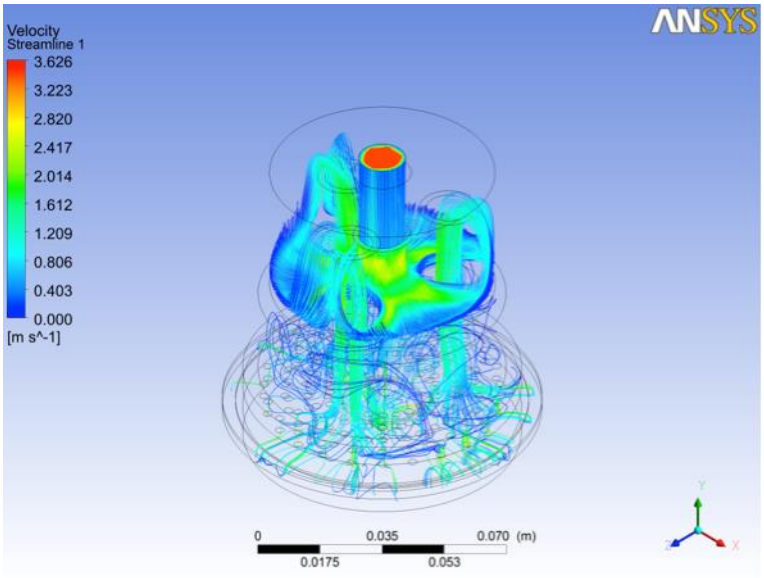

Figure 12 Velocity streamlines in Preseparator and Stage 0

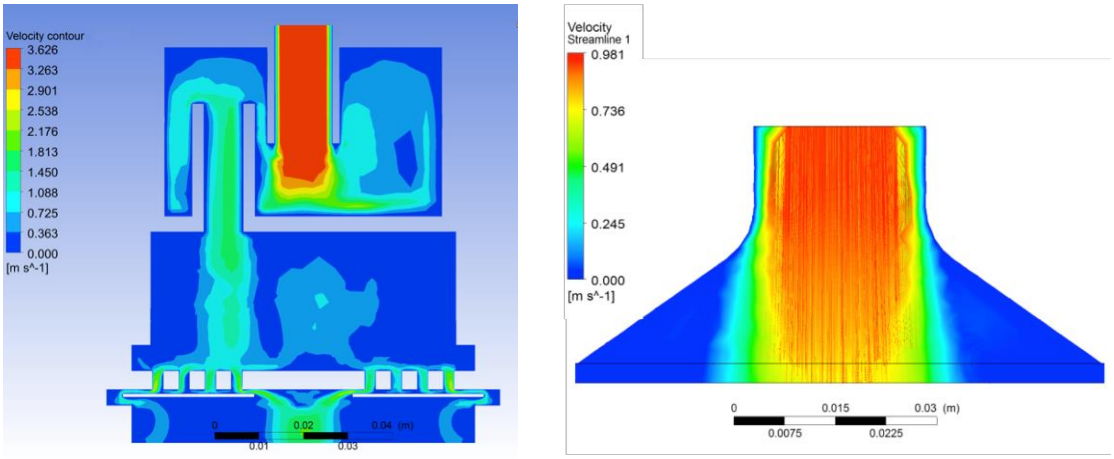

a) Preseparator b) Traditional USP metal inlet

Figure 13 Velocity contour plot of preseparator (a) and traditional USP inlet (b)

From the contour plot in Figure 13, the air velocity was accelerated near to the preseparator's middle sheet (up to 3.71±0.09 and 8.68±0.16 m/s at the 28.3 and 60 L/min flow rate, respectively). The streamline turned around the preseparator's orifice and drove continuously to the preseparator's outlet. Therefore, the preseparator inlet acted as a particle sizer in a similar way to what happens at the lower stage's

nozzle and where the B plate is the collection plate. The regions with more than a 90º bend produced the recirculation zone. The velocity profiles in the vertical portion of the ex-preseparator ACI seem to be less skewed than in the add-on preseparator ACI model (Figure 12). The reduction in the velocity gradient was expected to cause an increase in the turbulent viscosity associated with the downstream propagation to the connection tube of the preseparator (Longest et al., 2008). It means that those air recirculation zones were observed at the center of the preseparator, above the orifice, and it was predominant after exiting the orifice. These regions have a low velocity. The other 10-micron sized particles were trapped at stage 0. The streamline was observed to strike the collection plate of the preceding stage (Stage 0), then flowed through the 180º bend, and entered the connection section leading to the nozzle plate. Moreover, the airflow was observed as the flow field was passing through the holes of the collection plates before further transitioning to the filter stage. Recirculation zones were observed in the air streamline on reaching stage 0. This flow pattern induced the recirculation of the particles that was dependent on their diameter and disturbed the separation process-taking place at the exit of the nozzle (Sethuraman and Hickey, 2001).

The velocity streamline of stage 0 shows different clustering patterns of high velocity when compared with the velocity streamline in the traditional induction port (Figure14a, 14b), which exhibited higher airflow velocity than that in the preseparator (Figure 14c, 14d) at both flow rates (28.3 and 60 L/min) conditions. These phenomena might be explained by larger outlet cavity of the preseparator compared by induction port. The airflow velocity distributions were 0.390±0.273 and 0.856±0.60 m/s (at 28.3 and 60 L/min) at stage 0. On the other hand, the traditional induction port generated higher airflow velocity that caused the separation flow stream at the corner of the cone. Then an annular region where a portion of the flow recirculates was created, resulting in a pressure loss in this region (Donovan et al., 2012).

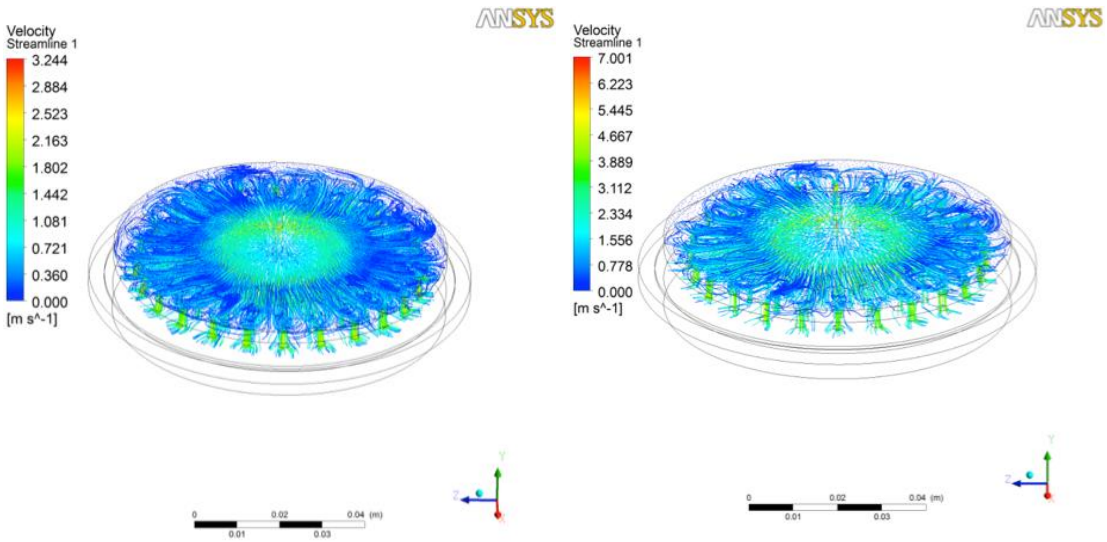

a) Under traditional USP metal inlet at 28.3 L/min

b) Under traditional USP metal inlet at 60 L/min

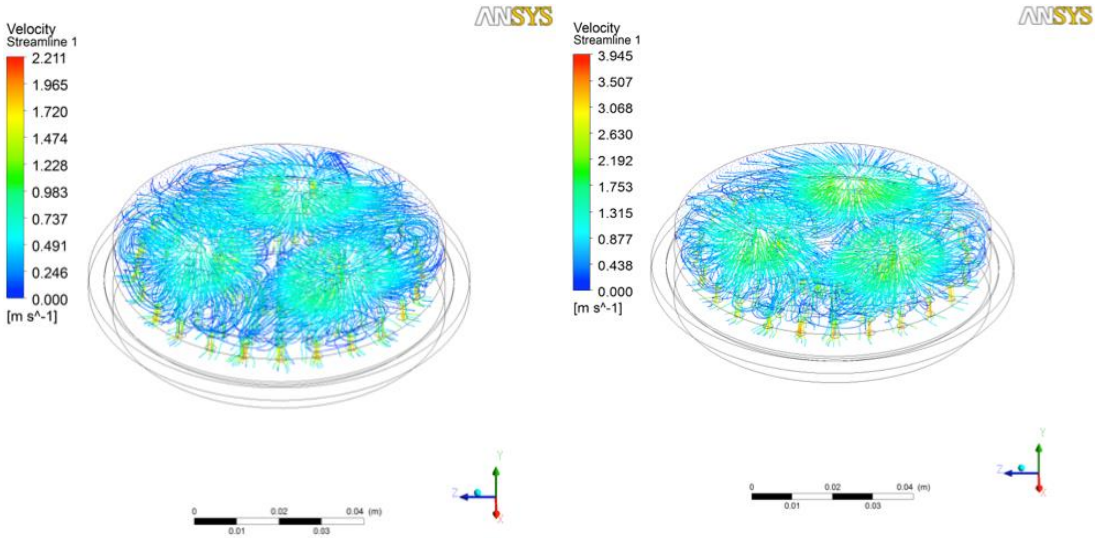

c) Under Preseparator at 28.3 L/min

d) Under Preseparator at 60 L/min

Figure 14 Velocity streamlines in Stage 0 under different inlet

According to Figure 15, the predicted numerical nozzle velocities were compared at each frame. At stage 2 and 3, the nozzle velocities increased along the frame (from peripheral to the centre of the collection plate). Therefore, the centre of the collection plate trends to trap larger particles with a high population of the particles. On the other hand, smaller particles (with in size of cut-off diameter on the stage) were accelerated by the nozzles of peripheral frame to deposit on the periphery of the collection plate. The smaller particles (not in the size range) were continuously moved and were further accelerated to the next stage of the ACI (Bardin-Monnier et

al., 2008). This assumption was supported by the particle acceleration in air streamline (Stokes equation). Moreover, two-dimension simulation showed similar recirculation streamline pattern at the outer wall of each stage.

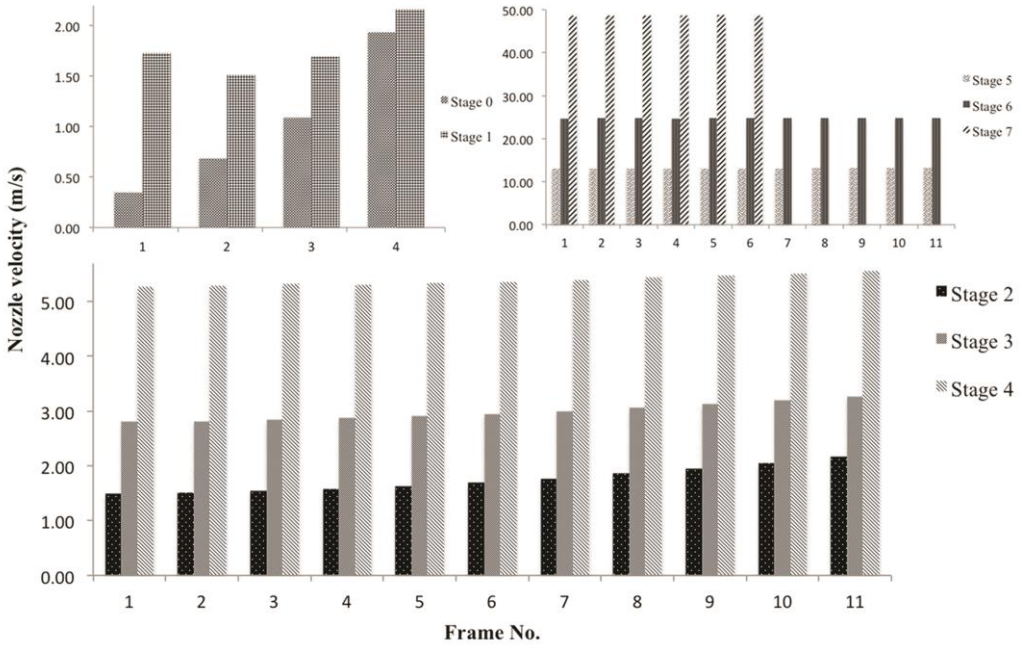

Figure 15 Computational predicted nozzle velocities on each frame of each stage at 28.3 L/min

4.2.4 Wall shear stress

These two models (preseparator and ex-preseparator) overcame the limitations of the previous model by exploring the effect of the flow from the preseparator to the flow through the stages (Sethuraman and Hickey, 2001; Gulak et al., 2009). According to Figure 16, the wall shear stress on the collection plate was presented on both the preseparator and the ex-preseparator. The three airflow streams, the air flow from the three connection tubes of the preseparator, reached stage 0 by passing through the nozzle that caused a spreading pattern of the wall shear stress grouping of “radius like” at the stage’s collection plate. The cone of the ex-preseparator model that affected the spreading pattern by continuously spread from the center of the collection plate. The increased velocity of air travels around the outer edges of the collection plates affected a wall shear characteristic with a higher

velocity nozzle area to cause a wider radius spread and a higher intensity of the wall shear. The wall shear stress on the collection plate ranged from 0.08 to 0.34 Pa (at 28.3 L/min of flow rate) and 0.11 to 0.37 Pa (at 28.3 L/min of flow rate) under the preseparator and the ex- preseparator produced air inlet, respectively. In addition, the preseparator showed a reduction of wall shear stress intensity on the collection plate inlet when compared to that of the ex-preseparator inlet (Figure 16).

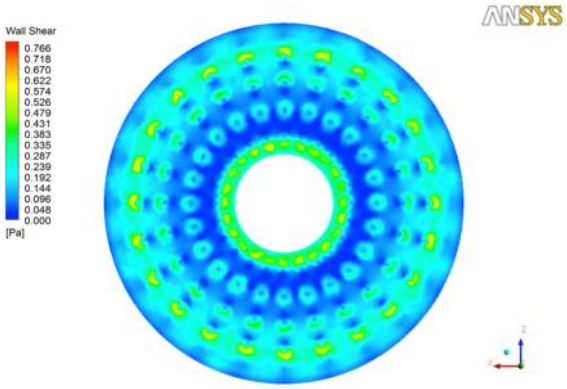

a) Wall shear stress distribution under traditional USP metal inlet

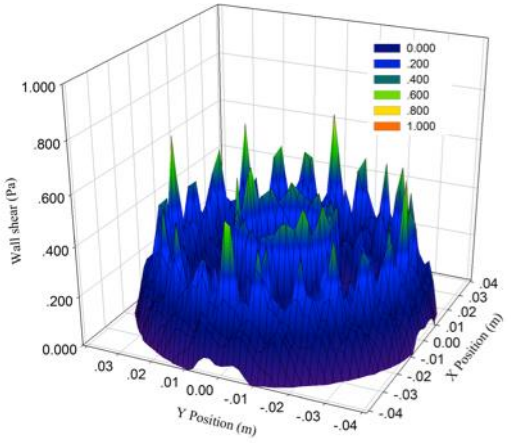

b) Wall shear stress intensity under traditional USP metal inlet

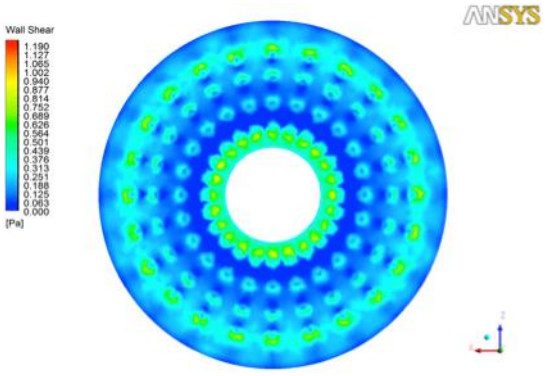

c) Wall shear stress distribution under Preseparator

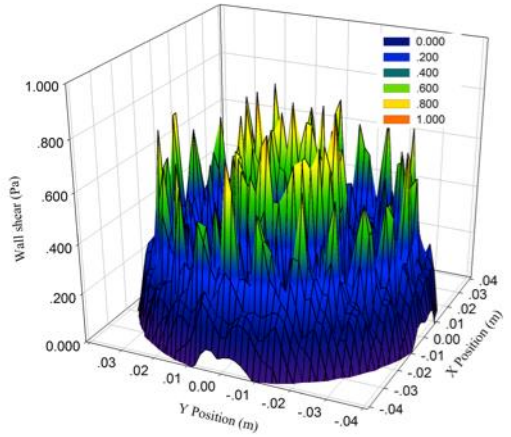

d) Wall shear stress intensity under Preseparator

Figure 16 The distribution and intensities of wall shear stress on collection plate of stage 0 under each inlet at 28.3 L/min.

The wall shear stress, which related to the drag intensity in the fluid flow against the wall, represents the viscous energy loss within the flowing boundary layer. In ideal of stationary wall, the isothermal pressure was reduced in a moving

fluid within an increment of length due to fluid friction (Figure 17). By increasing the Reynolds number, it was possible to locate a wider stagnation region where the fluid flow velocity was proposed to be zero (it means that the flow direction was readily transformed).

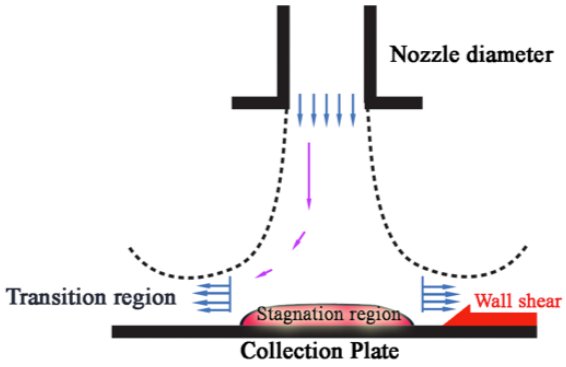

Figure 17 Schematic diagram of stagnation region and wall shear act on flow direction

These wall shear stresses caused the "ring like" zone of high intensity wall shear stress around the stagnation region under each nozzle. Moreover, the wall shear stress also explained the detachment and re-entrainment of the particles by that there was a critical value of the wall shear stress and the exposed time to react on those particles (Detry et al., 2009; Detry, 2007).

Therefore, the preseparator could reduce the trapped particles to re-entrain back into the stream flow. Then, the percentage wall loss of the impactor might be decreased, due to the decreased air velocity and smooth on the wall shear stress (Kamiya et al., 2009). It was found that particle removal depended on the shear stress even when it was not a linear correlation, for which the particle removal phenomena needs to have a critical wall shear stress (Young et al., 2013).

4.3 Calibrant characterizations and Particle size distributions

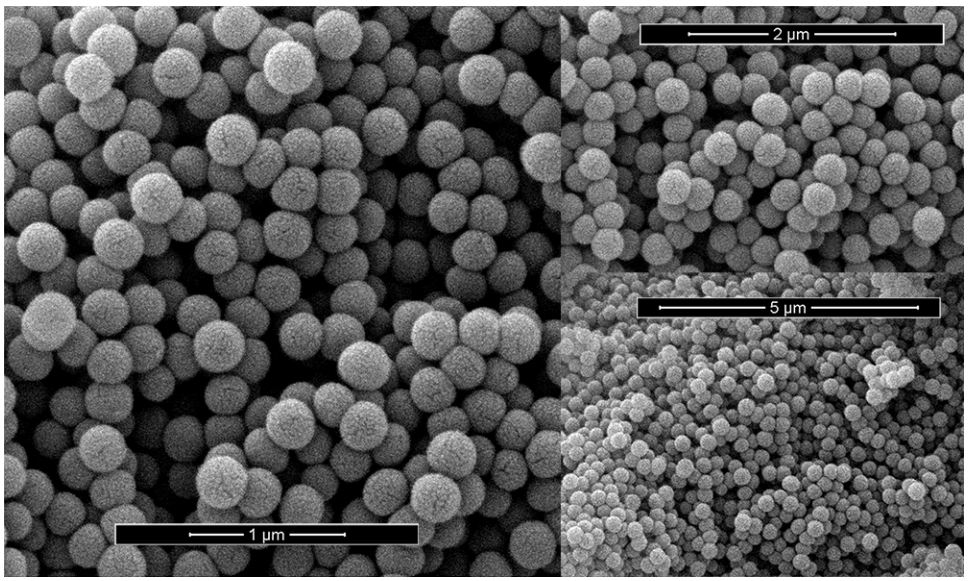

a) Monodisperse silica microsphere size 0.261 µm

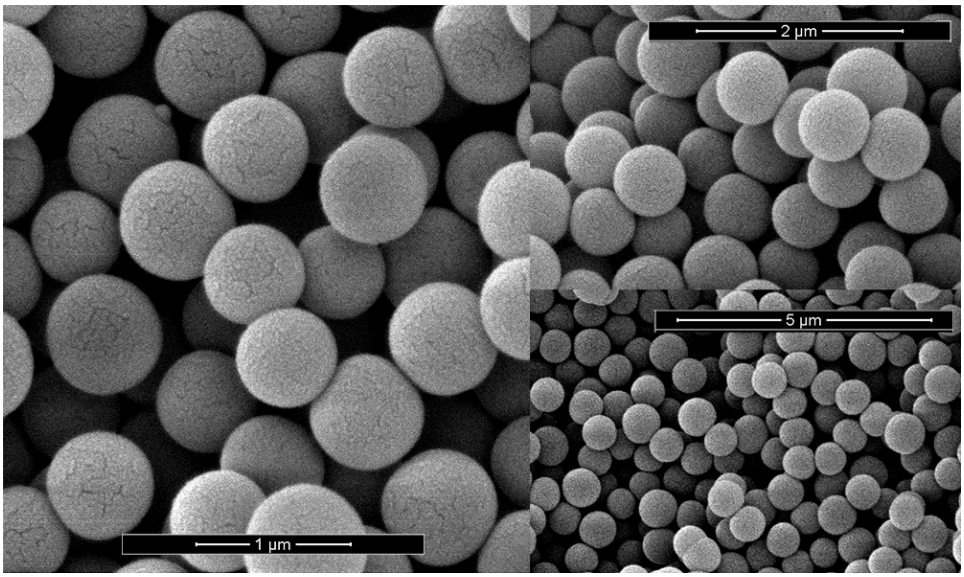

b) Monodisperse silica microsphere size 0.690 µm

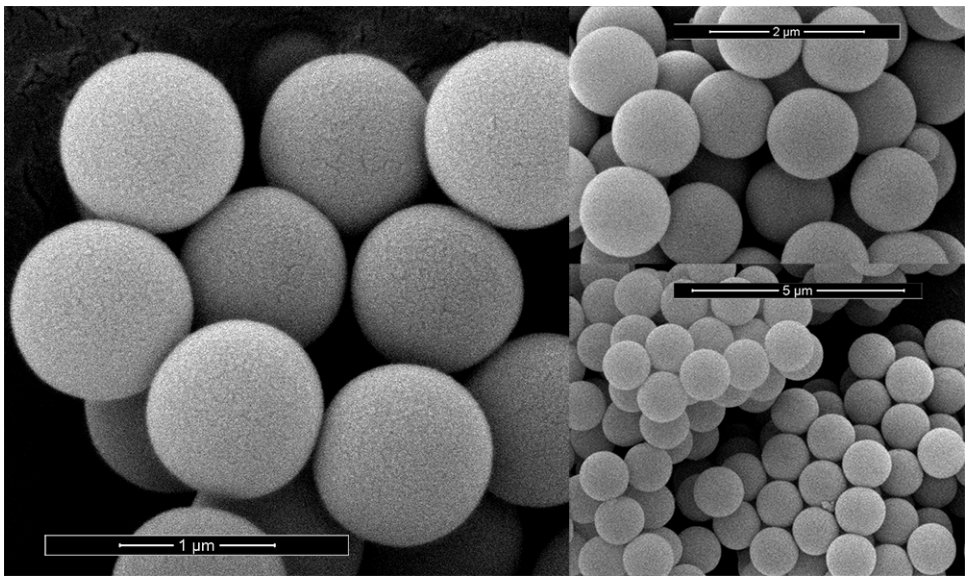

c) Monodisperse silica microsphere size 1.18 µm

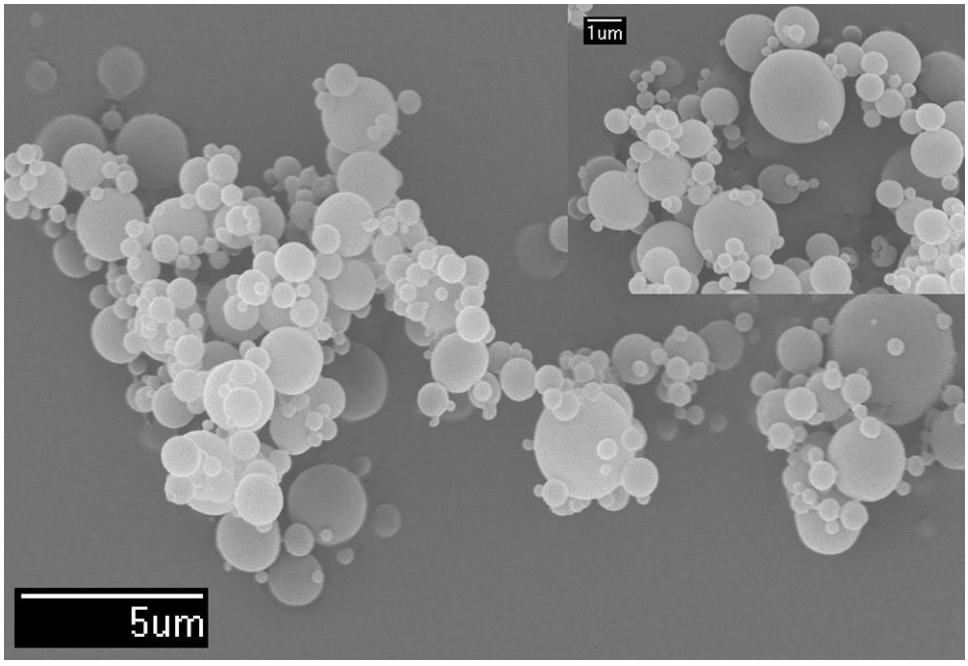

d) Spray-dried mannitol using mini spray dryer

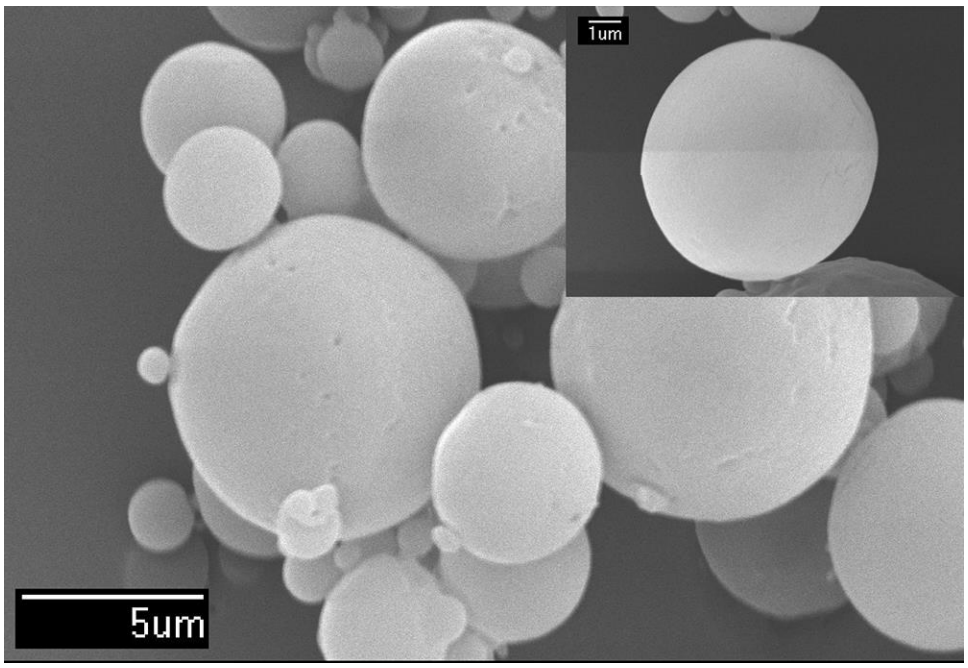

e) Spray-dried mannitol using Nano spray dryer

Figure 18 Morphology and surface characteristic of monodisperse silica microsphere and spray-dried mannitol under SEM

4.3.1 Particle morphology and surface characteristics

Figure 18 shows the morphology and surface of monodisperse silica microsphere and spray-dried mannitol under SEM. All monodisperse silica microsphere particles exhibited perfectly spherical shape and smooth on the surface with a specific size as labeled (0.261 μm, 0.690 μm and 1.18 μm). PSDs of silica microsphere showed completely mono disperse in each size range. The spray-dried mannitol using spray dryer and Nano spray dryer also presented perfectly spherical shape with smooth surface. However, PSDs revealed that there were various particle sizes in the spray-dried mannitol. All calibrant mannitol particles were successfully produced by spray-dried techniques then powders were collected from collection chamber of spray dryer and stored in a controlled temperature at 25 °C and 50 % relative humidity storage until use.

4.3.2 Spray-dried mannitol particle size

Particle size of calibrant particle was first characterized by Laser diffraction technique via Spraytec® and Mastersizer. The PSD was introduced into computer simulation and compared with particle distributions of each stage of ACI results after introduction of calibrated particles into the ACI.

Table 7 Particle size of the spray-dried mannitol measured by Laser diffraction technique (n=3)

	Spraytec® 60 lpm with metal throat		Dry powder cell Mastersizer	
	Mean (µm)	SE	Mean (µm)	SE
$Dv_{(0.5)}$	3.53	0.05	2.45	0.03
$Dv_{(0.9)}$	8.62	0.38	5.19	0.08
$Dv_{(0.1)}$	0.92	0.27	0.75	0.01
Span	2.18	0.01	1.81	0.01

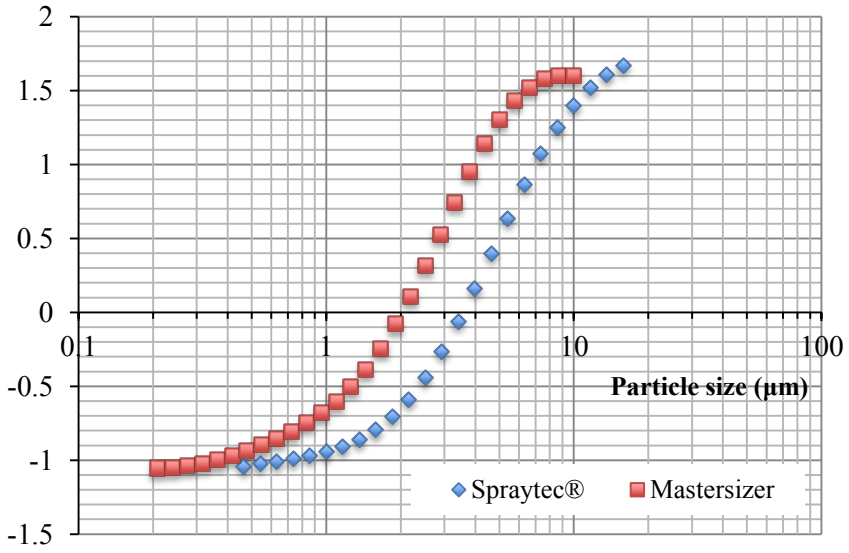

Figure 19 Particle size distribution of spray-dried mannitol using Spraytec® and Mastersizer

Table 7 and Figure 19 present the PSD of the spray-dried mannitol measurement by Spraytec® and Mastersizer. The trend of PSDs performed by 2 techniques appeared in a similar manner to each other. The curve shifting between techniques showed the difference in the median size. According to Table 7, the spray-

dried mannitol gave the PSD as polydisperse with median size at 3.53 and 2.45 μm and span equal to 2.18 and 1.81, respectively. The Mastersizer gave a smaller median size about 1 μm. The reason is that Mastersizer was operated using up to 4-bar of pressure with vibrating sample cell while Spraytec® was operated with 60 L/min of airflow passed through a dry powder device. It means that the de-agglomeration of Mastersizer given to the dry powder was higher than Spraytec®. Therefore, the agglomerated particle were broken in higher degree using Mastersizer (Ding and Riediker, 2015; Miansari et al., 2015). These results exemplified that Mastersizer is not suitable to be used in particle size measurement in comparison with the ACI calibration. Because the airflow rate at 60 L/min is enough for ACI operation to evaluate a normal dry powder inhaler.

4.4 Particle size distribution in ACI

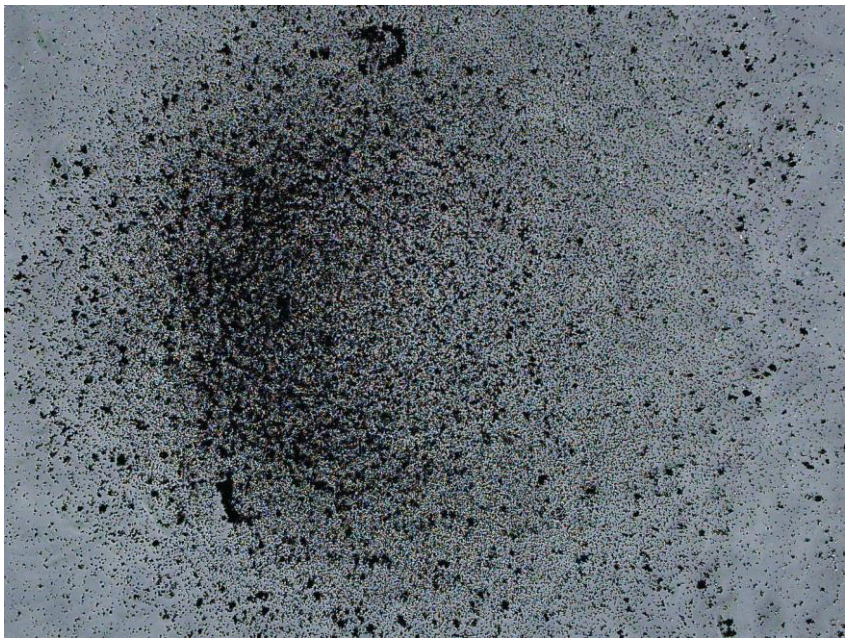

a) Trapped particles on collection plate under 1st frame nozzle of stage 0 (40x).

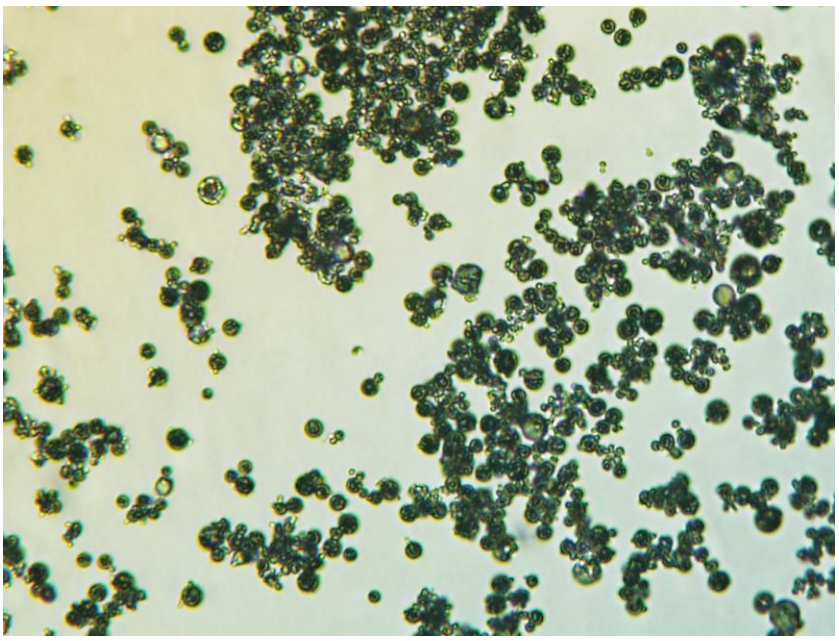

b) Agglomerated particles trapped on stage 0 ‘s collection plate (500x).

Figure 20 Spray-dried mannitol particles trapped on stage 0’s collection pate under light microscope

4.4.1 Projected particle size

The agglomeration of original particles may be occurred during the ACI measurement. Figure 20 shows the trapped particles on the adhesive disc under light microscope. The agglomerated particles have been grouped to larger particle and would be trapped on the early stages (Figure 20a). However, the real individual particle hasn’t changed under the microscope (Figure 20b). According to the microscopic cut-off, a gradient of particle size distribution decreased at lower stages, where stage 6 had 0.78 μm of particle geometric mean diameter, which might be the microscopic limitations.

The geometric mean diameters provided by microscopic technique are shown in the Table 8. A polydisperse spray-dried mannitol had distributed and deposited on collection plate of the cascade impactor according to their aerodynamic size. The geometric mean diameter (d_g) of particle on stage 0 was close to the cut-off size with manufacturer’s data. The other stages provided the deviated cut-off sizes from the actual values. However, all geometric mean diameters have shown good

correlation with the manufacturer's cut-off diameter. Table 8 also provides geometric mean diameters based on weight basis (d'_g). The d'_g describes the PSD based on weight fraction data. All d'_g at stages gave larger than d_g in mean diameters. Stage -1 to stage 3 exhibited well correlation with the manufacturer's cut-off diameter. These results justify the use of polydisperse aerosols to determine the stage's cut-off diameter of impactor.

Table 8 Geometric mean diameter on a weight basis using Hatch-Choate equation of microscopic technique (μm)

Stage	d_g	σ_g	Log d_{ln}	d'_g
S-1	7.79	0.84	0.90	8.53
S0	5.57	0.82	0.75	6.27
S1	3.96	0.89	0.60	4.12
S2	2.77	0.81	0.45	3.16
S3	1.89	0.83	0.28	2.10
S4	1.40	0.78	0.16	1.68
S5	1.06	0.78	0.04	1.28
S6	0.78	0.79	-0.10	0.92

d_g is a geometric mean diameter

σ_g is a geometric standard deviation

d_{ln} is a length-number mean diameter

d'_g is a geometric mean diameter on weight basis

4.4.2 PSD by Small cell laser diffraction

The particle distributions using single condition showed that there were particle sizes on each stage close to the original particle size (after spray-dried). It might be individual particles tend to be agglomerated by cohesive force that formed a larger size and trapped on the upper stage, which has the larger cut-off size. However, when the small cell laser diffraction had been operated the de-agglomeration occurred during the measurement process, that deagglomeration and particle breaking into single particles was measured resulting in not much different on

particle size distribution between stages. The PSD using single condition was characterized by the Mastersizer. The PSD of each stage exhibited no differences among stages, starting from the stage 3 to the preseparator.

The results indicated that $Dv_{(0.5)}$ showed no correlation with the result from the laser diffraction to the ACI using polydisperse mannitol particles (single condition). However, it has been shown that the particle size distribution of non-sonicated samples presented almost larger in size than the sonicated samples as shown in Table 9.

According to Table 9, the small cell laser diffraction was not appropriate for measuring the PSD on ACI collection plate using spray-dried mannitol. The breaking of dry particle should be considered. Moreover, the technique required large amount of sample to signal the sensor.

Table 9 PSDs on each stage of single condition spray-dried mannitol measured by small cell laser diffraction with/without sonication

Stages	$Dv_{(0.1)}$		$Dv_{(0.5)}$		$Dv_{(0.9)}$		Span	
	SN	nSN	SN	nSN	SN	nSN	SN	nSN
Dv	1.64	1.39	4.40	5.12	9.04	10.58	1.66	1.80
Mi	1.55	1.06	5.82	6.25	12.64	12.97	1.91	1.91
Pre	1.49	1.17	4.64	4.27	9.20	173.35	1.66	38.76
S-1	1.69	1.43	4.53	4.87	9.97	35.78	1.78	6.89
S0	1.63	1.28	4.87	4.84	10.16	9.80	1.69	1.76
S1	1.84	1.63	5.13	5.71	10.02	10.97	1.52	2.71
S2	1.78	1.82	4.02	6.36	8.49	13.48	1.65	2.71
S3	1.80	1.76	7.08	7.53	74.53	22.18	7.49	2.71

*S4-S6 there is inadequate of %obscuration to measure the particle distribution by this technique.

4.4.3 PSD of mixed spray-dried mannitol

Mixed spray-dried mannitol as calibrant were composed of 4 individual spray-dried mannitol in different conditions (A-D). Each condition has a

specific PSD as evaluated by laser diffraction technique (Spraytec®). There were 3.02, 3.91, 7.02, and 9.59 μm of mean median diameter. Therefore, each individual spray-dried mannitol gave a specific PSD. From Stage -1 to Stage 3, four different spray-dried mannitol conditions (A-D) were introduced to the ACI separately. Particle depositions on each plate depended on the stage cut-off diameter and particle inertial force, which related directly to their size.

The particles with enough inertial force were trapped on a collection plate. The PSD on each stage was described in Table 10. The errors of calibration were calculated as a relative accuracy (RAC). The % RAC were 90.36 to 106.03 when compared with the manufacturer's data (A to S3= 133.81 %, B to S2= 104.36, C to S0=106.03 % C to S1=100.48 %, D to S-1= 90.36 %).

The result shows that using spray-dried mannitol as a calibrant have been proved to be used for specific stage where the median size of spray-dried mannitol was close to their manufacturer's data. Nevertheless, lower stages, which have very small cut-off size, were not possible to calibrate with the spray-dried mannitol.

4.4.4 PSD of Monodisperse silica microsphere

Table 10(b) shows the mean Z-average and Peak 1 with standard error (SE) in term of trapped PSD on the collection plate. The spherical shape silica particle had been selected to be as calibrant for 3 lower stages (stage 4 to stage 6). Three-size ranges of silica particle (0.261, 0.690 and 1.180 μm) were introduced into the ACI (n=5). On stage 4, all silica microspheres exhibited Z-average close to the manufacturer's data with RAC of 71.41 % to 127.55 %, where PDI was in the acceptable range. Silica microspheres of 0.261 μm and 0.690 μm gave a good correlation on particle size collected on stage 5 with 94.40 % and 106.25 % of RAC, respectively. However, there was less correlation for 1.180 μm on stage 5. All silica microspheres gave un-correlated between manufacturer's cut-off diameters with PSD on stage 6 based on Z-average particle diameters. As another point of view, Peak 1 represented the highest intensity of particle size population, which is a good representative for a sample of unacceptable PDI. It shows a good correlation between data calibrated by silica microspheres and manufacturer's data as shown in Table 10.

Especially, peak 1 on stage 6 gave excellent correlation with 106.90 % and 90.85 % of RAC for 0.261 and 0.690 μm of silica microspheres, respectively.

In brief, the laser diffraction results showed good correlations between the PSD on each collection plate to the cut-off diameter of each stage. Even the definition of the cut-off diameter is the fraction of particle population that fifty percent of the specific size particle could be passed through the stage and another couldn't (Nichols et al., 1998; Srichana et al., 1998; Garmise and Hickey, 2008). The PSD on each stage gave exact particle that will be present on the collection of each stage.

Table 10(a) PSD of spray-dried mannitol (A-D) and measured particle size on each stage after introducing the formulations compared with the manufacturer's data as % relative accuracy (%RAC) and standard error (SE).

		Spray-dried mannitol							
		A		B		C		D	
Median		3.02		3.91		7.02		9.59	
STD		0.04		0.04		0.55		0.17	
Stage Ideal **		Mean/SE	%RAC	Mean	%RAC	Mean/SE	%RAC	Mean/SE	%RAC
S-1	9	5.46/0.14	60.67	-		7.60/0.04	84.44	8.13/0.05	**90.33**
S0	5.8	4.80/0.01	82.76	4.79/0.09	82.59	6.15/0.14	**106.03**	6.81/0.10	117.41
S1	4.7	3.55/0.14	75.53	4.12/0.08	87.66	4.72/0.06	**100.43**	5.31/0.03	112.98
S2	3.3	3.08/0.02	**93.33**	3.44/0.16	**104.24**	4.10/0.13	124.24	-	-
S3	2.1	2.81/0.18	**133.81**	2.94/0.21	140.00	-	-	-	-

*Bold number: Measured particle sizes close to cut-off diameter obtained by Manufacturer's data

** Ideal: Manufacturer's data

Table 10(b) PSD of monodisperse micro-sphere silica particle on stage 4 to stage 6 and the correlation of Z-average and Peak 1 compared with manufacturer's data as % relative accuracy (%RAC) and standard error (SE).

PSD on each stage (nm)		Micro-sphere Silica particle (μm)					
		0.261		0.69		1.18	
		Mean/SE	%RAC	Mean/SE	%RAC	Mean/SE	%RAC
Stage 4	Z-average	975.8 146.33	**88.70**	785.6 79.92	71.41	1403.1 105.86	127.55
	PDI	0.37		0.15		0.62	
	Peak 1	1112.6 327.9	101.14	822 78.58	74.73	620.6 133.22	56.42
Stage 5	Z-average	660.8 120.52	**94.40**	743.7 27.15	**106.25**	1979.3 96.78	282.76
	PDI	0.25		0.37		0.89	
	Peak 1	586.3 124.01	83.75	540.5 34.03	77.22	255.4 38.86	36.48
Stage 6	Z-average	669.9 139.8	167.47	1233.9 194.4	308.48	2335.2 323.56	583.80
	PDI	0.37		0.66		0.89	
	Peak 1	427.6 122.04	**106.90**	363.4 34.39	**90.85**	210 31.62	52.51

*Bold number: Measured particle sizes close to cut-off diameter obtained by Manufacturer's data

4.5 Particle travelling and particle deposition simulation

To study the particle traveling in the ACI, monodisperse and polydisperse particles were tracked along the model (60 L/min set). The most important aersol parameter is aerodynamic diameter that can be presented by the MMAD using specific cut-off diameter of the cascade impactor, where cut-off diameter obtained from the % collection efficiency curve of each stage (Graseby-Andersen, 1985).

The collection efficiency curves of computational simulation were obtained by individual particle injection from 0.3 to 11 μm of particle size. The 50 % collection efficiency seems to fit with manufacturer's data. The collection efficiency

of each stage showed continuing cumulative from the particle size that smaller than a specific cut-off diameter. Then the curves rapidly change at particle size, which is close to the stage cut-off size. Finally, the accumulation rate reached plateau phase at the particle size larger than the specific cut-off of each stage. Figure 21 exhibits clearly separated collection efficiency curve. The curves independently exhibited the 50 % collection efficiency and gave the cut-off diameter as good as the manufacturer's data.

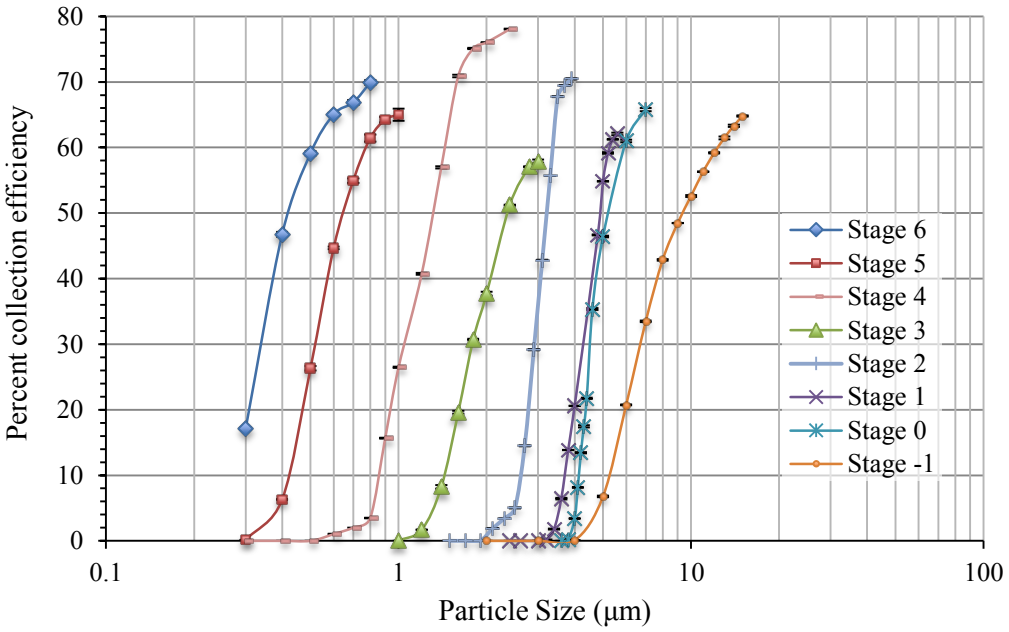

Figure 21 Numerical collection efficiency on each collection plate

To compare PSD between laboratories with computational data and to study the particle traveling in the ACI, the %mass distribution of the specific distribution of polydisperse calibrant particle was analyzed with the ACI and installed to CFD software as an initial PSD. The amounts of spray-dried mannitol on each stage were analyzed with LC RI detector (ACI condition: 20 mg of mannitol was placed into Plastic device, Run ACI 60 L/min for 10 sec) are shown in Figure 22, where the amount of mannitol that deposited on the device, metal inlet and the preseparator were neglected. The MMAD of the spray-dried mannitol was 4.08 μm with GSD at 1.75 for 60 L/min.

Figure 22 shows simulated PSD based on mass fraction of individual outlet of each stage using mass fraction of spray-dried mannitol converted by Rosin-Rammler's parameters then injected into CFD model. The simulated mass fraction at outlet of stage -1 exhibited the 50 % of particle size was around 4 µm. Then the mass fractions at 50 % were decreasing in size along lowering stage due to reducing cut-off size of each stage.

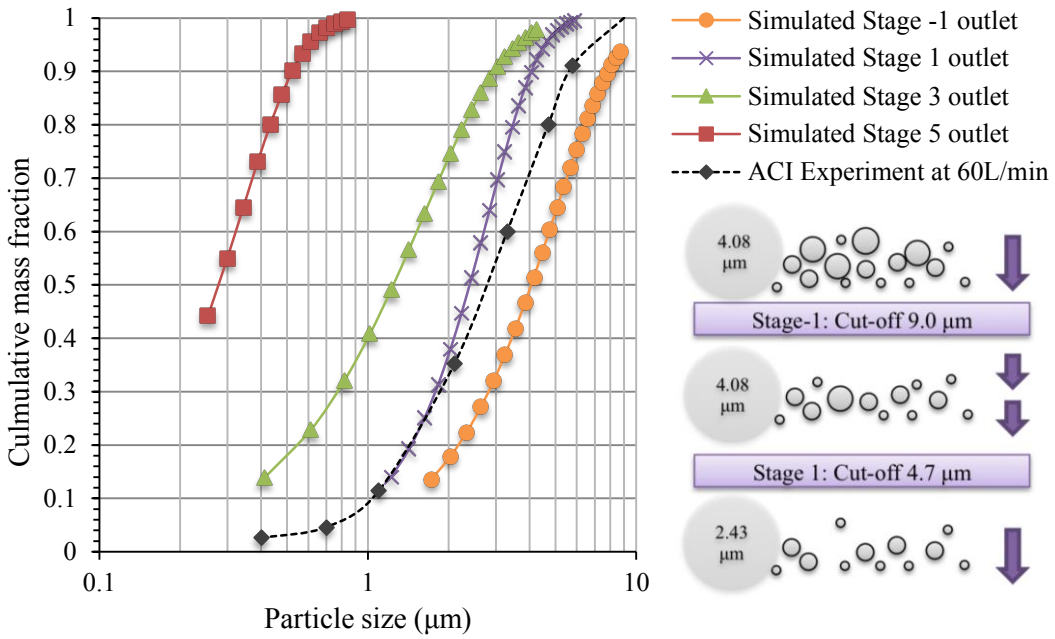

Figure 22 Mass fractions on each size of particle at the outlet of individual stage

According to the particle distribution of the calibrant, which had MMAD at 4.08 µm (at 60 L/min of airflow), most population of particle size based on mass was around 4.15 µm at outlet stage -1, which has cut-off diameter at 9 µm. This PSD characteristic had been carried on from inlet part till the stage 3 that has cut-off diameter smaller than it's MMAD. Then the mass fraction of particle size, which further flows to the lower stage, shifted to be a smaller PSD to correlate with cut-off diameter of further stage. For example, mass fraction was found close to 1.20 µm at the outlet of stage 3 (cut-off diameter of stage 4 is 1.10 µm).

The simulation and Figure 23 explained how the mixed spray-dried mannitol travelled in the ACI as the calibrant. Even if the calibrant particle was not the perfect monodisperse particle, it was trapped on the specific collection plate.

Therefore, it will lead to the idea of combination of all monodisperse particles as a single calibrant for ACI calibration (Srichana et al., 1998). The idea using mixed mono-/polydisperse as calibrant has described by Figure 23.

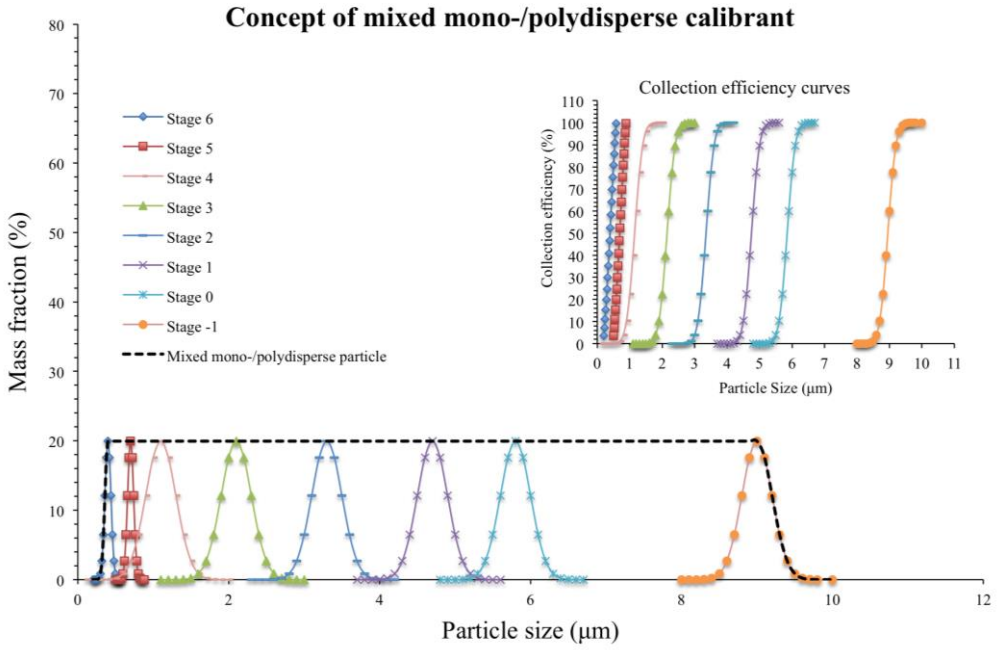

Figure 23 Concept of mixed mono-/polydisperse calibrant

The individual monodisperse particle has been calibrated an impactor for every single stage. The inconveniences of separating calibration are time consuming and high labor cost. The mixed mono-/polydisperse calibrant could be introduced into impactor at once to reduce the time of impactor cleaning and operation. The particles will express their behavior according to their aerodynamic size. So, the calibrant, which has PSD covered from 0.4 to 9 µm, possibly contributes to the good collection efficiency curves of each stage as shown in Figure 23.

4.6 Particle size distribution comparison

Figure 24 shows the cut-off size diameter of each stage among different measuring techniques with error bar. There are comparable results where some techniques produced high error. Microscopic technique exhibited slightly higher error than the others. Giving an overestimate at lower stages might be as a result of

the instrument limitation. For the upper stages (stage 3 to Stage-1), it had shown the underestimation.

In addition, using the mixed spray-dried mannitol (4 conditions) and silica microspheres gave comparable data via both laser diffraction and laser scattering techniques, which measured the particle distribution in different media (measuring particle in air (PIA) and Particle in Liquid (PIL), respectively). Even though there is a limitation in measuring a submicron particle by the laser diffraction, the laser scattering technique had been performed to overcome the limitation. Overall of the calibration data gave similar trend with the manufacturer's cut-off diameter data.

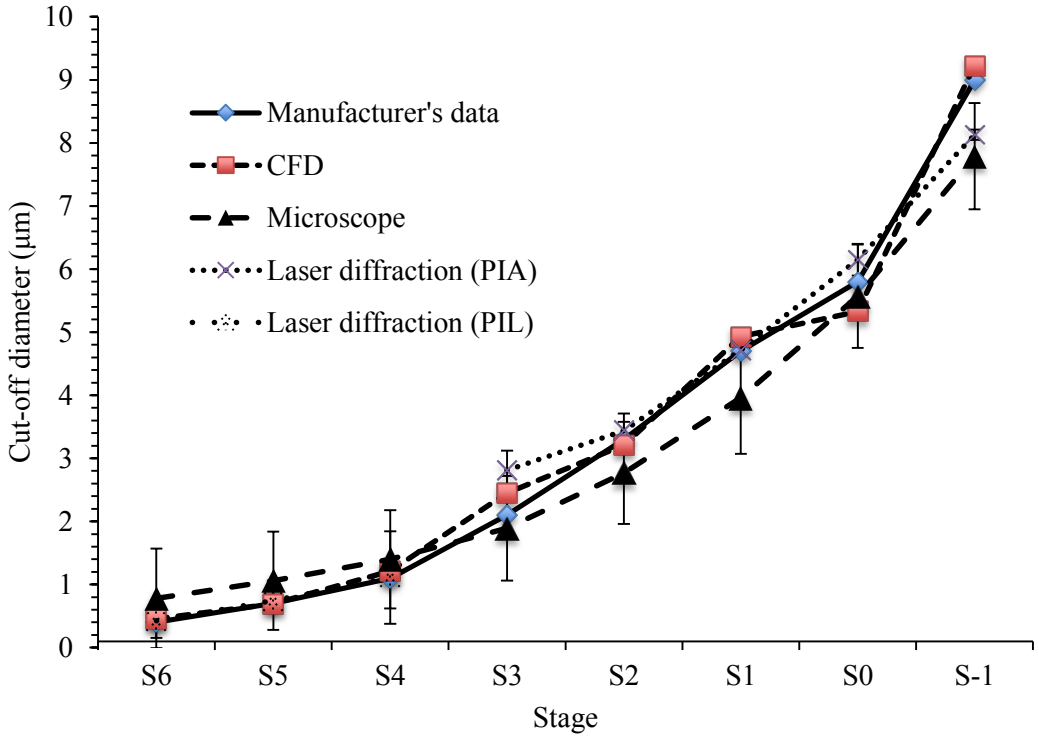

Figure 24 The comparison cut-off diameter of each stage using different techniques at 60 L/min

This PSDs comparison explained the performance of PSD determination technique when compared with manufacturer's data. There are many computational research works that compared stage cut-off diameter of impactor. The simulated results gave good correlations with experimental data from stage 0 to stage

7 using the flow rate at 28.3L/min (Flynn SJ et al., 2015; Gulak Y et al., 2009). For this study, the simulations focused mainly on dry powder inhaler using 60L/min of flow rate. Therefore, Stage -1 of ACI also was investigated with ACI set to determine the cut-off diameter via computational simulation. The simulated cut-off diameter provided close relation with manufacturer's data for the small size range but become more different at upper stage. The differences are possibly due to the limitation of the model.

CHAPTER 5
CONCLUSION

In conclusion, the current investigation illustrates the utility of a CFD model to describe the airflow characteristics of the aerosol testing equipment. Results of this study can be used for the better understanding of the airflow principle in traditional and equipped preseparator applications of the ACI. The preseparator's airflow indicated that airstreams travelled over the preseparator wall and ran down to the next stage. Accelerating the air velocity of the preseparator inlet proposes to persuade trapping of large particles on the preseparator's plate. However, the recirculation zone is possible to reduce wall-lose of dry powder formulations and only the preseparator recirculation zone was shown clearly in this study, where other was difficult to figure out. Moreover, wall shear stress was reduced in the preseparator equipped model. Future applications of the developed ACI model include evaluating the drug and particle size effect on deposition and quantifying the consequences of the aerosol. The CFD approach illustrated in this study can be used to design and develop the next generation aerosol assessment and characterization devices

The mono and polydisperse particles were analyzed and introduced to the ACI successfully. The spray-dried mannitol and silica microsphere offered suitable properties (smooth surface, perfect spherical shape and preferred PSD) to be used as a calibrant. This study presented the particle travelling in the cascade impactor with both experimental and computational results based on dry powder particulate system. The small particles tend to agglomerate together to form a larger particle size, which could be trapped on the beginning part of ACI. However, the most of particles still expressed their behavior. The simulated data explained the PSD of particle traveled along the ACI. The PSD was changed its mass fraction when the particles reached the appropriate stage cut-off diameter. At this point, the particles, which has larger diameter than stage's cut-off diameter, were trapped on collection plate. Then the changed PSD had been flown to further stage.

The calibration cut-off diameter was changed from the old definition that every point of particle collection efficiencies was obtained by mass fraction of

individual size on collection plate compared with the whole cascade impactor. Therefore, this study carried the PSD on each stage to be a representative for the stage cut-off diameter. The other particle sizing technique such as laser diffraction technique or microscopic technique showed good correlations with the manufacturer's cut-off data using both mono and polydisperse dry powder system. In addition, the particle breaking phenomenon and sample needed for instrument should be considered during PSD analysis.

Using mixed mono-/polydisperse calibrant has been performed in this research and produced the satisfied results. The PSDs comparison demonstrates the feasibility of the calibrant. However, the microscopic data gave error at the end of ACI according to microscopic limitation. The computational simulation exhibited very good correlation with the manufacturer's cut-off diameter. Moreover, the simulation of particle traveling confirmed calibration results. The idea of using poly-disperse dry powder introduced into the ACI has been confirmed, which can reduce time and labour consuming process.

BIBLIOGRAPHY

Abouali O, Saadabadi S, Emdad H. 2011. Numerical investigation of the flow field and cut-off characteristics of supersonic/hypersonic impactors. *J Aerosol Sci*, 42, 65–77.

Adi H, Young PM, Chan H-K, et al. 2010. Co-spray-dried mannitol–ciprofloxacin dry powder inhaler formulation for cystic fibrosis and chronic obstructive pulmonary disease. *Eur J Pharm Sci*, 40, 239–247.

Andersen A. 1966. A sampler for respiratory health hazard assessment. *Am Ind Hyg Assoc J*, 27, 160–165.

Bailey AG, Balachandran W, Williams TJ. 1983. The rosin—rammler size distribution for liquid droplet ensembles. *J Aerosol Sci*, 14, 39–46.

Bardin-Monnier N, Falk V, Marchal-Heussler L. 2008. Computational Fluid Dynamics: A tool to the formulation of therapeutic aerosols. *Computer Aided Chemical Engineering*, 25, 823-828

Barnocky G, Davis RH. 1988. The effect of Maxwell slip on the aerodynamic collision and rebound of spherical particles. *J Colloid Interface Sci*, 121, 226–239.

Cohen JJ, Montan DN. 1967. Theoretical considerations, design, and evaluation of a cascade impactor. *Am Ind Hyg Assoc J*, 28, 95–104.

Dechraksa J, Suwandecha T, Maliwan K, Srichana T. 2014. The Comparison of Fluid Dynamics Parameters in an Andersen Cascade Impactor Equipped With and Without a Preseparator. *AAPS PharmSciTech*, 15, 792–801.

Detry JG. 2007. Computation and evaluation of wall shear stress distribution at the lower surface of a radial flow cell. *International Requirement Engineering Conference (RE)*.

Detry JG, Jensen BBB, Sindic M, Deroanne C. 2009. Flow rate dependency of critical wall shear stress in a radial-flow cell. *J Food Eng*, 92, 86–99.

Ding Y, Riediker M. 2015. A system to assess the stability of airborne nanoparticle agglomerates under aerodynamic shear. *J Aerosol Sci*, 88, 98–108.

Donovan MJ, Kim SH, Raman V, Smyth HD. 2012. Dry powder inhaler device influence on carrier particle performance. *J Pharm Sci*, 101, 1097–1107.

Duan Q, An J-L, Wang H-L, Miao Q. 2014. Pollution characteristics of organic and elemental carbon in atmospheric particles in Nanjing northern suburb in summer. *Huanjing KexueEnvironmental Sci*, 35, 2460–2467.

Flesch JP, Norris CH, Nugent Jr AE. 1967. Calibrating Particulate Air Samplers with Monodisperse Aerosols.: Application to the Andersen Cascade Impactor. *Am Ind Hyg Assoc J* , 28, 507–516.

Flynn SJ, Tong ZB, Yang RY, et al. 2015. Computational fluid dynamics (CFD) investigation of the gas-solid flow and performance of Andersen cascade impactor. *Powder Technol*, 285, 128–137.

Garmise RJ, Hickey AJ. 2008. Calibration of the Andersen cascade impactor for the characterization of nasal products. *J Pharm Sci*, 97, 3462–3466.

Graseby-Andersen. 1985. Operating manual for Andersen 1 ACFM non-viable ambient particle sizing samplers. Andersen Instruments Incorporated, Atlanta, GA

Gulak Y, Jayjock E, Muzzio F, et al. 2009. Numerical calibration of the Andersen cascade impactor using a single jet model. *Int J Pharm*, 377, 45–51.

Hassan MS, Lau R. 2011. Inhalation performance of pollen-shape carrier in dry powder formulation: effect of size and surface morphology. *Int J Pharm*, 413, 93–102.

Instruments M. 2007. Spraytec User Manual MAN0368.

Kamiya A, Sakagami M, Byron PR. 2009. Cascade impactor practice for a high dose dry powder inhaler at 90 L/min: NGI versus modified 6-stage and 8-stage ACI. *J Pharm Sci*, 98, 1028–1039.

Kwon SB, Lim KS, Jung JS, et al. 2003. Design and calibration of a 5-stage cascade impactor (K-JIST cascade impactor). *J Aerosol Sci*, 34, 289–300.

Levitzky MG. 2013. Chapter 1. Function and Structure of the Respiratory System. In: Pulmonary Physiology, 8e. The McGraw-Hill Companies, New York, NY,

Liu BY. 2012. Fine particles: Aerosol generation, measurement, sampling, and analysis. *Academic press*, New York, p. 311

Li Y, Zhang H, Qiu X, et al. 2013. Dispersion and risk assessment of bacterial aerosols emitted from rotating-brush aerator during summer in a wastewater treatment plant of xi'an, china. *Aerosol Air Qual Res*, 13, 1807–1814.

Longest PW, Hindle M, Das Choudhuri S, Xi J. 2008. Comparison of ambient and spray aerosol deposition in a standard induction port and more realistic mouth-throat geometry. *J Aerosol Sci*, 39, 572–591.

Longest PW, Vinchurkar S. 2007. Validating CFD predictions of respiratory aerosol deposition: effects of upstream transition and turbulence. *J Biomech*, 40, 305–316.

Lundgren DA. 1967. An aerosol sampler for determination of particle concentration as a function of size and time. *J Air Pollut Control Assoc*, 17, 225–229.

Marple VA, Liu BYH. 1974. Characteristics of laminar jet impactors. *Environ Sci Technol*, 8, 648–654.

Marple VA, Liu BY, Whitby KT. 1974. Fluid mechanics of the laminar flow aerosol impactor. *J Aerosol Sci*, 5, 1–16.

Marple VA, Willeke K. 1976a. Impactor design. *Atmospheric Environ 1967*, 10, 891–896.

Marple VA, Willeke K. 1976b. Inertial impactors: theory, design and use. Fine Part *Aerosol Generation Measurement Sampling Analysis*, New York, 412–446.

Matida EA, Finlay WH, Lange CF, Grgic B. 2004. Improved numerical simulation of aerosol deposition in an idealized mouth–throat. *J Aerosol Sci*, 35, 1–19.

Miansari M, Qi A, Yeo LY, Friend JR. 2015. Vibration-induced deagglomeration and shear-induced alignment of carbon nanotubes in air. *Adv Funct Mater*, 25, 1014–1023.

Mitchell J, Newman S, Chan H-K. 2007. In vitro and in vitro aspects of cascade impactor tests and inhaler performance: A review. *AAPS Pharmscitech,* 8(4), 237-248.

Moeller EH, Jorgensen L. 2008. Alternative routes of administration for systemic delivery of protein pharmaceuticals. *Protein Ther*, 5, e89–e94.

Morsi SA, Alexander AJ. 1972. An investigation of particle trajectories in two-phase flow systems. *J Fluid Mech*, 55, 193–208.

Nadarassan DK, Assi KH, Chrystyn H. 2010. Aerodynamic characteristics of a dry powder inhaler at low inhalation flows using a mixing inlet with an Andersen Cascade Impactor. Eur J Pharm Sci 39:348–354.

Nichols SC, Brown DR, Smurthwaite M. 1998. New concept for the variable flow rate andersen cascade impactor and calibration data. *J Aerosol Med Depos Clear Eff Lung*, 11, S133–S138.

Nichols SC, Mitchell JP, Shelton CM, Roberts DL. 2013. Good cascade impactor practice (GCIP) and considerations for “in-use” specifications. *AAPS PharmSciTech*, 14, 375–390.

Rader DJ, Mondy LA, Brockmann JE, et al. 1991. Stage response calibration of the Mark III and Marple personal cascade impactors. *Aerosol Sci Technol,* 14, 365–379.

Sethuraman VV, Hickey AJ. 2001. Evaluation of preseparator performance for the 8-stage nonviable andersen impactor. *AAPS PharmSciTech*, 2(1), 34-52.

Srichana T, Juthong S, Thawithong E, et al. 2014. Clinical equivalence of budesonide dry powder inhaler and pressurized metered dose inhaler. *The clinical respiratory journal,* 10(1), 74-82.

Srichana T, Martin GP, Marriott C. 1998. Calibration method for the Andersen cascade impactor. *J Aerosol Sci*, 29, S761–S762.

United States Pharmacopeial Convention. 2015. Usp39-Nf34. *United States Pharmacopeia*

Vinchurkar S, Longest PW, Peart J. 2009. CFD simulations of the Andersen cascade impactor: Model development and effects of aerosol charge. *J Aerosol Sci,* 40, 807–822.

Walters DK, Cokljat D. 2008. A three-equation eddy-viscosity model for Reynolds-averaged Navier–Stokes simulations of transitional flow. *J Fluids Eng*, 130, 121401.

Worth Longest P, Vinchurkar S. 2007. Validating CFD predictions of respiratory aerosol deposition: Effects of upstream transition and turbulence. *J Biomech,* 40, 305–316.

Young RM, Hargather MJ, Settles GS. 2013. Shear stress and particle removal measurements of a round turbulent air jet impinging normally upon a planar wall. *J Aerosol Sci*, 62, 15–25.

APPENDIX

User defined function

```
/************************************************************************
***
      UDF for specifying steady-state parabolic pressure profile boundary
      profile for a turbine vane edit to inlet profile

************************************************************************
***/
   #include "udf.h"
   DEFINE_PROFILE(turbulent_inlet_profile, t, i)
{
  real z, x, del, hx, hz, y[ND_ND], ufree, XMAX, XMIN, ZMAX, ZMIN,
DELOVRH, UMEAN, B;
  face_t f;
  hx = XMAX - XMIN;
  del = DELOVRH*hx;
  hz = ZMAX - ZMIN;
  del = DELOVRH*hz;
  ufree = UMEAN*(B+1.);
  begin_f_loop(f,t)
/* constants  */
f = 0.045;
/* variable declarations */
    {
      F_CENTROID(y,f,t);
      x = y[1];
      if (x <= del)
        F_PROFILE(f,t,i) = ufree*pow(x/del,B);
      else
        F_PROFILE(f,t,i) = ufree*pow((hx-x)/del,B);
    }
  end_f_loop(f,t);
  begin_f_loop(f,t)
```

```
/* constants  */
f = 0.045;
/* variable declarations */
    {
     F_CENTROID(y,f,t);
     z = y[2];
     if (z <= del)
       F_PROFILE(f,t,i) = ufree*pow(z/del,B);
     else
       F_PROFILE(f,t,i) = ufree*pow((hz-z)/del,B);
    }
  end_f_loop(f,t);
   }

/*****************************************************************
***** UDF to apply the kinetic energy criterion for each collection plate in DPM
calibration.
NOTE: some portions of the code structure were appropriated from Example 1 of
Section 2.5.1.3 in the ANSYS 13.0 UDF Manual. (* reflect boundary condition for
inert particles *)
*****************************************************************
*****/
#include "udf.h"
#include "math.h"
DEFINE_DPM_BC(bc_collection_ke,p,t,f,f_normal,dim)
{
  real alpha;  /* angle of particle path with face normal */
  real vn=0.;
  real nor_coeff = 1.;
  real tan_coeff = 0.3;
  real ke = 0.;
  real normal[3];
```

```
  int i, idim = dim;
  real NV_VEC(x);
  double kedesire;

#if RP_2D
  /* dim is always 2 in 2D compilation. Need special treatment for 2d
     axisymmetric and swirl flows */
  if (rp_axi_swirl)
    {
     real R = sqrt(p->state.pos[1]*p->state.pos[1] +
                   p->state.pos[2]*p->state.pos[2]);
     if (R > 1.e-20)
       {
        idim = 3;
        normal[0] = f_normal[0];
        normal[1] = (f_normal[1]*p->state.pos[1])/R;
        normal[2] = (f_normal[1]*p->state.pos[2])/R;
       }
     else
       {
        for (i=0; i<idim; i++)
          normal[i] = f_normal[i];
       }
    }
  else
#endif
    for (i=0; i<idim; i++)
     normal[i] = f_normal[i];
  /* calculate the normal component, rescale its magnitude by
        the coefficient of restitution and subtract the change */
                  alpha = M_PI/2. - acos(MAX(-1.,MIN(1.,NV_DOT(normal,p-
>state.V)/
```

```
                        MAX(NV_MAG(p->state.V),DPM_SMALL))));
    if ((NNULLP(t)) && (THREAD_TYPE(t) == THREAD_F_WALL))
      F_CENTROID(x,f,t);


  /* Compute normal velocity. */
    for(i=0; i<idim; i++)
      vn += p->state.V[i]*normal[i];
    /*calculate the kinetic energy*/
ke = 0.5*vn*vn*P_MASS0(p);
kedesire = 6.3119*pow(10,-14);
/*trap the particle*/
 if(ke > kedesire){return PATH_ABORT;}
 else //reflect particle
  {
    alpha = M_PI/2. - acos(MAX(-1.,MIN(1.,NV_DOT(normal,p->state.V)/
                        MAX(NV_MAG(p->state.V),DPM_SMALL))));
    if ((NNULLP(t)) && (THREAD_TYPE(t) == THREAD_F_WALL))
      F_CENTROID(x,f,t);

    /* calculate the normal component, rescale its magnitude by
       the coefficient of restitution and subtract the change */

    /* Compute normal velocity. */
    for(i=0; i<idim; i++)
      vn += p->state.V[i]*normal[i];

    /* Subtract off normal velocity. */
    for(i=0; i<idim; i++)
      p->state.V[i] -= vn*normal[i];

    /* Apply tangential coefficient of restitution. */
```

```
    for(i=0; i<idim; i++)
      p->state.V[i] *= tan_coeff;

    /* Add reflected normal velocity. */
    for(i=0; i<idim; i++)
      p->state.V[i] -= nor_coeff*vn*normal[i];

    /* Store new velocity in state0 of particle */
    for(i=0; i<idim; i++)
      p->state0.V[i] = p->state.V[i];

    return PATH_ACTIVE;
   }
  return PATH_ABORT;
}
```

VITAE

Name Mr. Janwit Dechraksa
Student ID 5310730001
Educational Attainment

Degree	Name of Institution	Year of Graduation
Bachelor of Pharmacy	Khon Kaen University	2010

Scholarship Awards during Enrolment

1. Thesis Grant, Education fee and Scholarship
   The Higher Education Research Promotion and National Research University Project of Thailand, Office of the Higher Education Commission.
2. Thesis Grant
   The Graduate School, Prince of Songkla University.
3. Thesis Grant
   The Nanotec-PSU Excellence Center on Drug Delivery Systems, Faculty of Pharmaceutical Sciences, Prince of Songkla University.
4. Conference Scholarship
   Faculty of Pharmaceutical Sciences, Prince of Songkla University.

List of Publication and Proceeding

Dechraksa, J., Maliwan, K. and Srichana, T. 2012. The use of computational fluid dynamic in an Andersen cascade impactor. *The 2nd Current Drug Development International Conference (CDD 2012),* Phuket Graceland Resort & Spa, Phuket, Thailand, May 2-4

Dechraksa, J., Suwandecha, T., Maliwan, K., Srichana, T. 2013. Computational Fluid Dynamic studies in the Andersen cascade impactor. *The Pulmonary and Intranasal Drug Delivery Conference, Inhalation Asia 2013*, Hong Kong, p. 13PS6. June 26-28,

Dechraksa J, Suwandecha T, Maliwan K, Srichana T. 2014. The comparison of fluid dynamics parameters in an Andersen cascade impactor equipped with and without a preseparator. *AAPS Pharm Sci Tech*. 1;15(3), 792-801.

Leung, S.S.Y., Tang, P., Zhou, Q.T., Tong, Z., Leung, C., Decharaksa, J., Yang, R. and Chan, H.K. 2015. De-agglomeration Effect of the US Pharmacopeia and Alberta Throats on Carrier-Based Powders in Commercial Inhalation Products. *The AAPS journal*, 17(6), 1407-1416.